Isolating Clusters of Light Elements in Molecular Sieves with Atom Probe Tomography

Joel E. Schmidt[1], Linqing Peng[2], Alessandra Lucini Paioni[3], Helena Leona Ehren[3], Wei Guo[4], Baishakhi Mazumder[4], D. A. Matthijs de Winter[5], Özgün Attila[1], Donglong Fu[1], Abhishek Dutta Chowdhury[1], Klaartje Houben[3], Marc Baldus[3], Jonathan D. Poplawsky[4,*], and Bert M. Weckhuysen[1,*]

[1]Debye Institute for Nanomaterials Science, Utrecht University, Universiteitsweg 99, 3584 CG Utrecht, The Netherlands. *Corresponding author, b.m.weckhuysen@uu.nl.

[2]Grinnell College, 1115 8th Ave, Grinnell, IA 50112, USA.

[3]NMR Spectroscopy, Bijvoet Center for Biomolecular Research, Utrecht University, Padualaan 8, 3584 CH Utrecht, The Netherlands.

[4]Center for Nanophase Materials Sciences, Oak Ridge National Laboratory, Oak Ridge, TN 37831, USA. *Corresponding author, poplawskyjd@ornl.gov.

[5]Structural Geology & EM, Utrecht University, Postbus 80.021, 3508 TA Utrecht, The Netherlands.

Contents

1. List of Movies

Movie S1. Analysis of heterogeneities in the coke distribution after the methanol-to-hydrocarbons (MTH) reaction with ^{13}C labelled methanol for needle 20. Views of all Si ions, all ^{13}C ions along with 7% ^{13}C isosurfaces in gray and ^{13}C clusters. Bounding box dimensions of 84 × 63 × 62 nm^3. These movies are of the needles from Figure 1.

Movie S2. Reconstruction of a representative SAPO-34 needle (needle 8). Bounding box dimensions 281 × 79 × 78 nm^3. These movies are of the needles from Figure S11.

Movie S3. Selected results of atom probe simulations as a function of Si island size (N_{Si}) and delocalization (σ). Each panel contains a 5 × 5 × 5 nm^3 view of all atoms that was removed from the center of the larger simulated data set, as well as a view only the Si atoms, with O in gray, tetrahedral atoms in green and Si in red. These samples are the same as those in Figure 2 and S21.

2. SAPO-34 Literature Survey

Microporous materials (MMs), also termed molecular sieves, are a compositionally diverse family of crystalline, heterogenous catalysts including zeolites (aluminosilicate composition) and aluminophosphates ($AlPO_4$'s).[1,2] $AlPO_4$ materials contain a framework structure of alternating Al^{3+} and P^{5+} oxide tetrahedra, to form a charge neutral framework, but the substitution of Si^{4+} into framework positions can create charge imbalances, leading to Brønsted acidity or ion exchange sites in the silicoaluminophosphate (SAPO) material. These materials have a long and rich history, though shorter than zeolites, as $AlPO_4$'s were first reported in 1982[3] and SAPO's in 1984.[4] In zeolites, the substitution of Al^{3+} into framework positions is governed by Löwenstein's rule, but Si^{4+} substitution is much more complex in SAPO-type materials. General bonding rules are that Si-O-Si, Si-O-Al, and Al-O-P bonds are allowed, and Al-O-Al, P-O-P, and Si-O-P bonds are not allowed, leading to a situation where Si islands of discrete sizes are formed, governed not only by bonding rules, but by the crystalline framework structure itself.[5,6] There are a few defined mechanisms of Si^{4+} substitution, where Si^{4+} can replace a single P^{5+} to form an isolated Si site (SM2 mechanism), or a Si-O-Si pair can substitute for an Al-O-P pair (SM3 mechanism), but this must happen in combination with the SM2 mechanism to form a Si island as Si-O-P bonds are forbidden.[5,6] These mechanisms were first established in the late 1980's, and much of the early understanding of Si substitution mechanisms came from SAPO-5 (AFI framework), SAPO-37 (FAU framework) and SAPO-34 (CHA framework).[6–15] While the basics of Si substitution were solved decades ago, more recent work has shown that this is a frustratingly complex process with heterogeneities that span length scales from an atomic bond (sub-nanometer) to zoning in a single crystal (microns), with influences on material performance.[5,16–31] The smallest island that can be formed is 5 Si atoms, and there is theoretically no upper limit to their size, and islands will form in discrete sizes dictated by the framework structure.[10,15,18,20,23,26,32,33] The substitution of Si has important catalytic implications as it influences the strength of the acid sites, as the Brønsted acid site strength decreases in the order of $Si(OAl)(OSi)_3$> $Si(OAl)_2(OSi)_2$ > $Si(OAl)_3(OSi)$> $Si(OAl)_4$, though not over a very wide range; additionally, the strength of the acid sites generally increases with increasing island size, and is also influenced by the location, distribution, accessibility and Si content.[5–7,10,22,24] This is difficult to control, and is a poorly understood function of organic template (structure directing agent), Si content, synthesis conditions, source of reagents, etc., but it is commercially vital as it dictates catalyst performance.[22,25,32,34–38]

Although many SAPO-type catalysts have been reported, perhaps the most studied is SAPO-34 (CHA framework topology which contains a 3-D system of 8-membered rings (MRs) that limit accessibility to larger internal cages). It has been applied commercially since 2010 in the methanol-to-hydrocarbons (MTH) process, even though the material was first reported in 1984, showing there may be several decades between material discovery and commercial use.[4,34,39,40] While the material is seemingly simple as the ideal CHA framework contains only a single T-site (triclinic $R\bar{3}m$ symmetry, space group No. 166)[41], the $AlPO_4$ and SAPO compositions have a number of reported symmetries that depend on the template, calcination, use of fluoride, Si content or degree of hydration, including $P\bar{1}$[42,43], P1[44], R3[44] and $R\bar{3}$[43]. From a practical perspective, one of the most important characteristics of the material is the active site distribution as this will have consequences on material performance. At the atomic scale, the Si^{4+} distribution is governed by bonding rules, and Si^{4+} can only exist as isolated species, $Si(OAl)_4$, or in islands of discrete sizes of 5, 8, 11, 14, and larger, Si atoms, as a consequence of the specific CHA framework structure.[28] At larger length scales a non-uniform distribution of Si has also been observed, with an increasing Si content from the crystal core to surface in a synthesis using diethylamine.[20] Additionally, sporadic Si zoning in the lamellar precursor to SAPO-34 synthesized using a dry gel conversion (DCG),[5] and potential aluminosilicate (zeolite) domains in the material have also been reported to contribute to a non-uniform Si distribution, but it is not clear if these findings can be generalized to all SAPO-34 materials as they have only been reported in very specific cases of SAPO-34 and large crystals of SAPO-5.[33,45] All of these complications highlight the complexity of SAPO-34, and a recent report from the Dalian Institute of Chemical Physics describes the tremendous amount of work that went into catalyst optimization before commercial application.[34]

Understanding the islands in SAPO-34 is vital to explaining its catalytic performance.[46,47] ^{29}Si magic angle spinning (MAS) solid-state nuclear magnetic resonance (ssNMR) spectroscopy provides a powerful method to characterize isolated Si and Si islands as it is able to sensitively and quantitatively probe the local environment of Si and distinguish between $Si(OSi)_4$, $Si(OAl)(OSi)_3$, $Si(OAl)_2(OSi)_2$, $Si(OAl)_3(OSi)$ and $Si(OAl)_4$ connectivities, and has been the default method to study and quantify isolated Si and Si islands in SAPO catalysts for decades.[11,48] However, ssNMR typically provides only averages over an entire sample, so no direct information about the 3-D spatial distribution of islands will be gained. Additionally, as ^{29}Si is < 5% of earth abundant Si it can be challenging to probe Si-Si correlations. Electron microscopies may be capable of resolving Si islands, however, to the best of our knowledge, these techniques have only been applied to monitor exchanged heteroatoms (e.g. Cu, Pt, Sn) or mesopores in SAPO-34.[49–52] Additionally, beam damage to MMs materials is common with these techniques, further complicating their application, though future advances in instrumentation may decrease beam damage.[53–55]

3. Synthesis of SAPO-34

Two different SAPO-34 samples were synthesized with both low and high Si contents from the following procedures.

High-Si SAPO-34

Following Karawacki and coworkers[56], high-silica SAPO-34 was prepared by mixing 0.80 g of Catapal B Alumina with 5.78 g of water and stirring for 5 min. Then 0.356 g of Cabosil M-5 fumed silica was added and the mixture was homogenized by magnetic stirring. Next, 1.34 g of 85% phosphoric acid was added and the solution homogenized, followed by 1.00 g of morpholine, and the resulting solution was mixed for 4 h, and had the following molar ratios: $1Al_2O_3$:$1.08SiO_2$:$1P_2O_5$:2.09Morpholine:$66H_2O$. The mixture was transferred to a 23 mL Teflon lined Parr autoclave and held at 200°C for 24 h, after which time the reactor was quickly cooled in cold water and the product recovered by centrifugation and evaluated by PXRD (Figure S1), confirming the CHA phase.

Low-Si SAPO-34

Low-silica SAPO-34 was synthesized following the procedure of Marchese and coworkers,[57] and adding a small amount of SiO_2. First, 0.80 g of Catapal B Alumina were mixed with 4.3 g of water and stirred for 5 min. Then 0.025 g of Cabosil M-5 fumed silica was added and the mixture was homogenized by magnetic stirring. Next, 1.27 g of 85% phosphoric acid was added and the solution homogenized, followed by the addition of 1.2 g of morpholine, and the resulting solution was mixed for 1 h. Finally, 1.4 g of a 2.76 M solution of HF was added (Caution: Use all necessary safety precautions when working with HF) to obtain a mixture with the following molar ratios: $1Al_2O_3$:$0.075SiO_2$:$1P_2O_5$:2.5Morpholine:0.7HF:$66H_2O$, and the solution was mixed with magnetic stirring for 1 h. The mixture was transferred to a 23 mL Teflon lined Parr autoclave and held at 200°C for 24 h, after which time the reactor was quickly cooled in cold water and the product recovered by centrifugation and evaluated by PXRD (Figure S2), confirming the CHA phase.

^{29}Si enriched samples

Samples enriched in ^{29}Si were prepared following the procedures above except that 99.69% ^{29}Si enriched $^{29}SiO_2$ (Isoflex USA) was used instead of Cabosil M-5 with no further modification. PXRD patterns are shown in Figures S3 and S4, confirming the CHA phase in each synthesis.

Calcination

All samples were calcined in a tube furnace under flowing air (100 mL / min) with the following program: Ramp to 150°C at 1 K/min and hold for 1.5 h, then ramp to 580°C at 1 K/min and hold for 6 h followed by cooling to room temperature.

4. Methanol-to-Hydrocarbons (MTH) reaction

Large crystals of SAPO-34 are the same as those reported by Karawacki and coworkers.[56] The crystals were calcined in a Linkam cell under a flow of pure O_2 with the following program: Ramp to 400°C at 15 K/min and hold for 30 min. Then ramp to 550°C at 5 K/min and hold for 210 min. The MTH reaction was then performed by first cooling the crystals to 500°C and switching to N_2 atmosphere. The nitrogen flow (20 mL/min) was then switched to a bubbler containing ^{13}C labeled methanol at room temperature (99 at. %, Sigma Aldrich, vapor pressure of ~100 mm Hg) and the reaction was run for 60 min. After the reaction finished the flow was switched back to only nitrogen and the reaction cell cooled to room temperature.

5. Powder X-ray Diffraction

PXRD was used to confirm phase purity of all as-made samples. Diffraction patterns were collected using a Bruker D2 Phaser (2nd Gen) using a cobalt radiation source, Co kα = 1.789 Å. Powdered samples were rotated at 15 revolutions/min. All diffraction patterns were normalized to the highest peak.

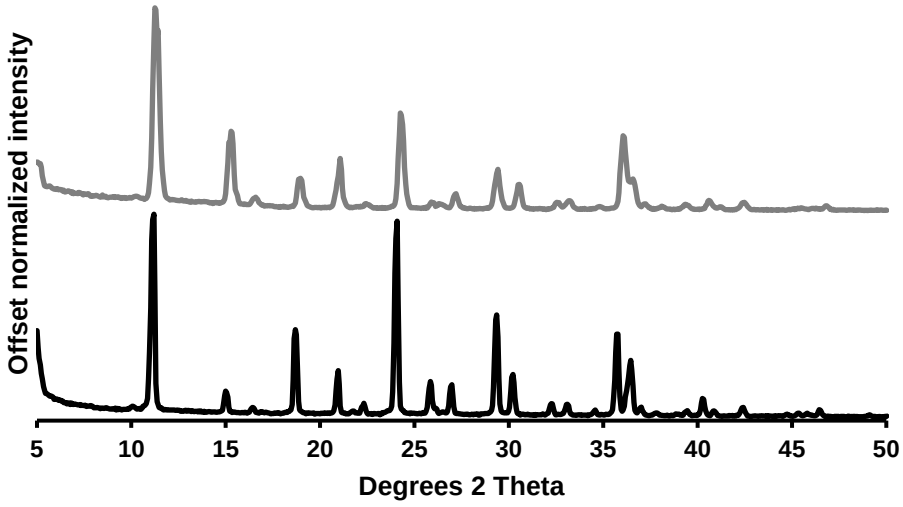

Figure S1. Powder X-ray diffraction patterns of sample 1 as-made (bottom) and calcined (top).

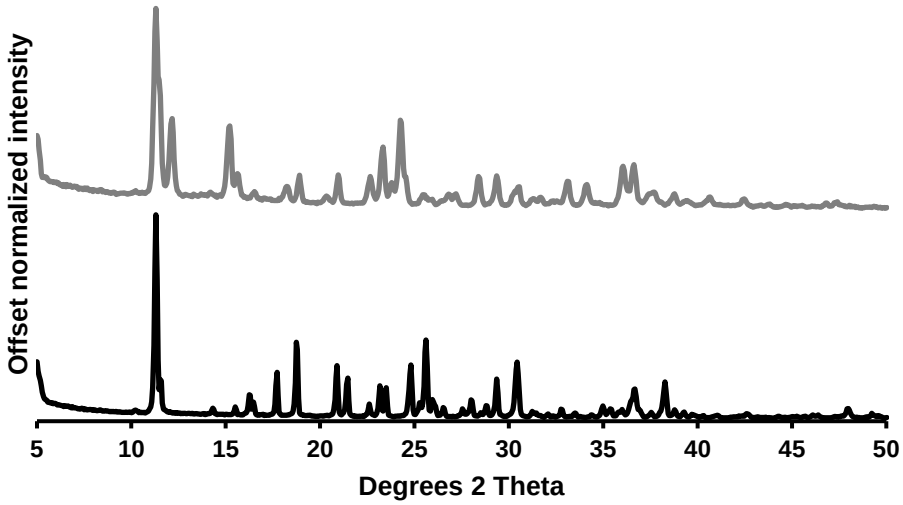

Figure S2. Powder X-ray diffraction patterns of sample 2 as-made (bottom) and calcined (top). Note that the change in the diffraction pattern after calcination and rehydration from ambient humidity is due to the known reduction in symmetry to space group P1.[44]

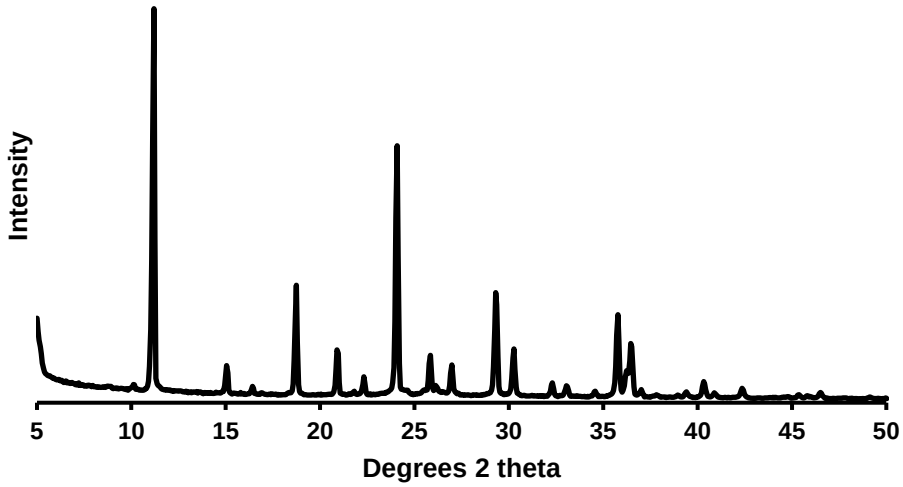

Figure S3. Powder X-ray diffraction patterns of sample 3 as-made.

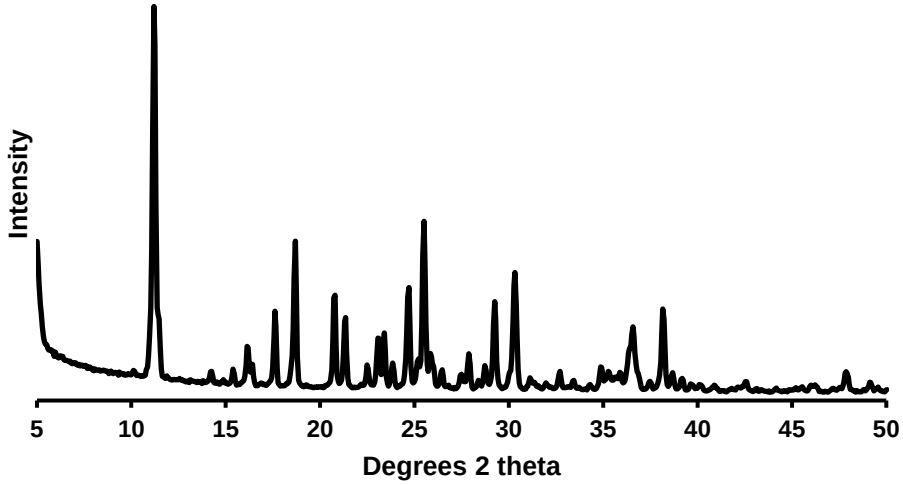

Figure S4. Powder X-ray diffraction patterns of sample 4 as-made.

6. ^{29}Si Magic Angle Spinning (MAS) Solid-State Nuclear Magnetic Resonance (ssNMR) Spectroscopy Deconvolutions

The materials were studied using ^{29}Si magic angle spinning (MAS) solid-state nuclear magnetic resonance (ssNMR) spectroscopy and all experiments were performed on a Bruker 500MHz wide-bore magnet with an AVANCE-III console and equipped with a 3.2 mm HXY probe in double channel ^{1}H, ^{29}Si mode. All experiments were performed at room temperature (298 K) and at a MAS frequency of 15 kHz. Referencing was done externally to TMS. ^{29}Si spectra were recorded using direct excitation (DE) and ^{1}H-^{29}Si cross polarization (CP) experiments. An RF field of 60 kHz was used for ^{29}Si DE spectra, acquired with 1024 scans and T_1 was used to determine the delay. For the ^{29}Si enriched samples, T_1 was 58 s and 16 s for the low and high Si samples, respectively, so delay times of 300 s and 90 s were used. For the unenriched samples a delay of 300s was used. The ^{1}H-^{29}Si CP spectra were recorded using 5s recycle delay and an accumulation of 8192 scans. Cross-polarization was achieved using a 54 kHz ^{29}Si field and 70% ramp during 3ms contact time. ^{1}H field strength during 90° pulses was 90 kHz and for SPINAL64 proton decoupling was 65 kHz.[58] Spectral processing was performed using 100Hz line broadening. All spectra were processed and analyzed with Bruker Topspin_3.5.

For ^{29}Si ssNMR the chemical shift determines the local Si environment, *i.e.* the number of Al or Si neighbors, and the generally accepted chemical shifts for SAPO-type materials and $Si(OSi)_4$, $Si(OAl)(OSi)_3$, $Si(OAl)_2(OSi)_2$, $Si(OAl)_3(OSi)$ and $Si(OAl)_4$ nearest neighbors are approximately -110, -105, -100, -95 and -92 ppm, respectively, with small changes dependent on the state of the material (template containing, calcined, rehydrated, reacted, etc.), and an additional peak around -115 ppm is also commonly assigned to $Si(OSi)_4$.[24,35,59,60] The ^{29}Si DE ssNMR spectra of samples 3-5 are shown in Figure S5, with a normalized comparison to the ^{29}Si and ^{1}H-^{29}Si CP spectra given, and these were the samples subsequently studied with APT. In Figure S7 to Figure S9 the absolute values of the ^{29}Si DE MAS spectra shown in Figure S5 are plotted so that the number of counts can be compared along with a deconvolution of the ssNMR spectra, with results in Tables S1 to S3. As is expected in the ^{1}H-^{29}Si CP spectra, the signal for $Si(OAl)_4$ is significantly enhanced as it will be near a proton to compensate for the charge imbalance. From the deconvolutions, it is apparent that all samples contain isolated Si as well as Si islands. Interestingly, all samples contain a majority of $Si(OSi)_4$ and $Si(OAl)_4$ environments, with only a few edge sites.

The signal enhancement gained by using isotopically enriched ^{29}Si is shown in Figure S6, which gives a comparison of the ^{29}Si DE spectra of natural abundance and enriched samples (samples 1-4). As this shows there is over an order of magnitude increase in signal intensity at an equal number of scans with isotopic enrichment. The ^{29}Si ssNMR spectra highlight the advantage and importance of using labeled Si to study SAPO-type materials, especially with low-Si contents. In the natural abundance sample the ^{29}Si MAS ssNMR spectra took over 500 h (21 days) to acquire to achieve a high signal to noise ratio, and a collection time this long would be impractical in most situations. However, once enriched ^{29}Si was used a spectrum with a superior signal to noise ratio could be collected in only 26 h, and even with the low-Si sample the measurement time was 85 h, still much less than 500 h (equal numbers of scans were used for both labeled materials but the relaxation delay times differed). In order to have a more direct comparison and highlight the advantage of ^{29}Si isotopically labeled Si, we compared syntheses of both high and low Si SAPO-34, with the only difference being the use of natural abundance fumed silica or ^{29}Si isotopically enriched silica. Samples 1-4 were studied using ^{29}Si DE ssNMR, with an equal number of scans used for each sample, and the results shown in Figure S6. The spectra show the expected increase in signal intensity due to the labelling, and simplify differentiating the Si environments.

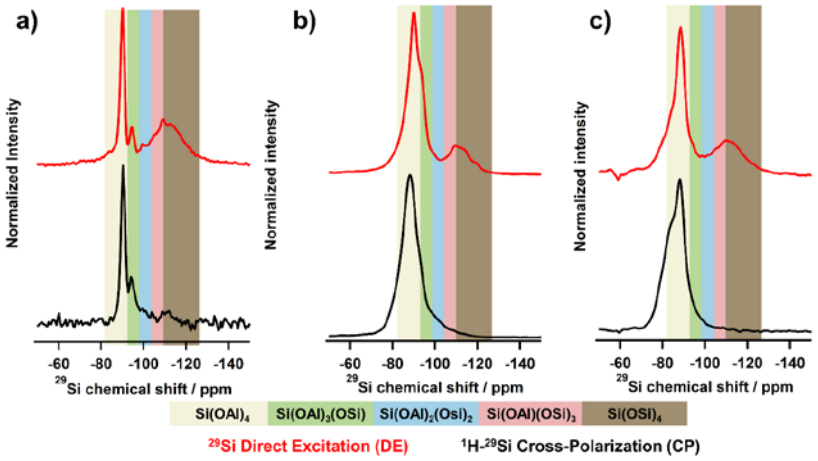

Figure S5. Normalized ^{29}Si direct excitation (DE, red traces) and ^{1}H-^{29}Si cross polarization (CP, black traces) magic angle spinning (MAS) solid-state nuclear magnetic resonance (ssNMR) spectra, along with highlighted regions corresponding to local Si bonding environments with a color legend at the bottom. Note that regions are deconvoluted as Gaussian functions so there will be overlap, which is why region widths are not uniform in this figure. For deconvolutions see Figures S7 to S9. a) Template containing large crystals of SAPO-34 (sample 5). For the DE spectra 5984 scans were collected with a relaxation delay time of 300 s. For the CP spectra 8192 scans were collected with a relaxation delay time of 4 s. b) Calcined ^{29}Si isotopically enriched high-Si SAPO-34 (sample 3). For the DE spectra 1024 scans were collected with a relaxation delay time of 90 s. For the CP spectra 8192 scans were collected with a relaxation delay time of 5 s. c) Calcined ^{29}Si isotopically enriched low-Si SAPO-34 (sample 4). For the DE spectra 1024 scans were collected with a relaxation delay time of 300 s. For the CP spectra 8192 scans were collected with a relaxation delay time of 5 s.

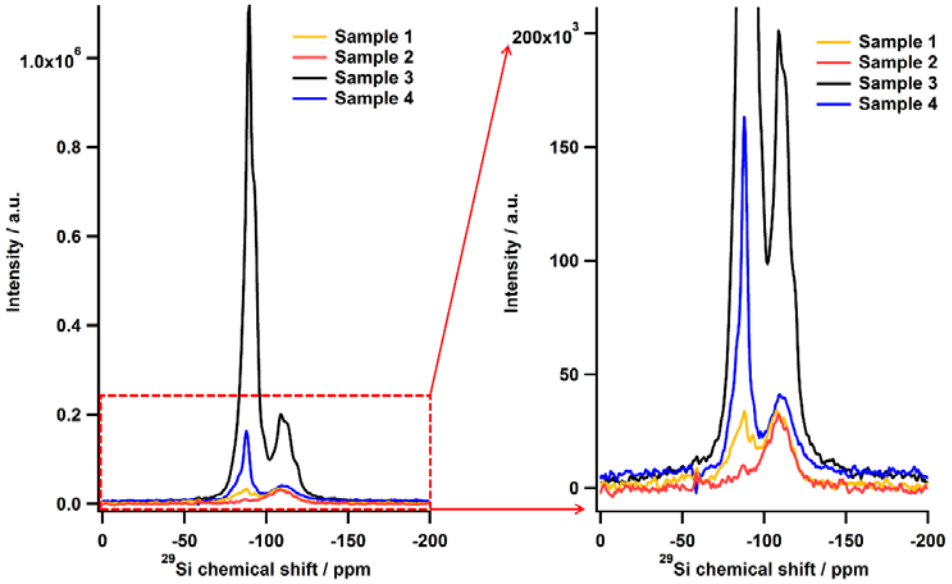

Figure S6. Demonstration of the signal enhancement of the ^{29}Si direct excitation (DE) solid-state nuclear magnetic resonance (ssNMR) spectra, from using ^{29}Si isotopically labeled ^{29}Si. For all samples 1024 scans were collected.

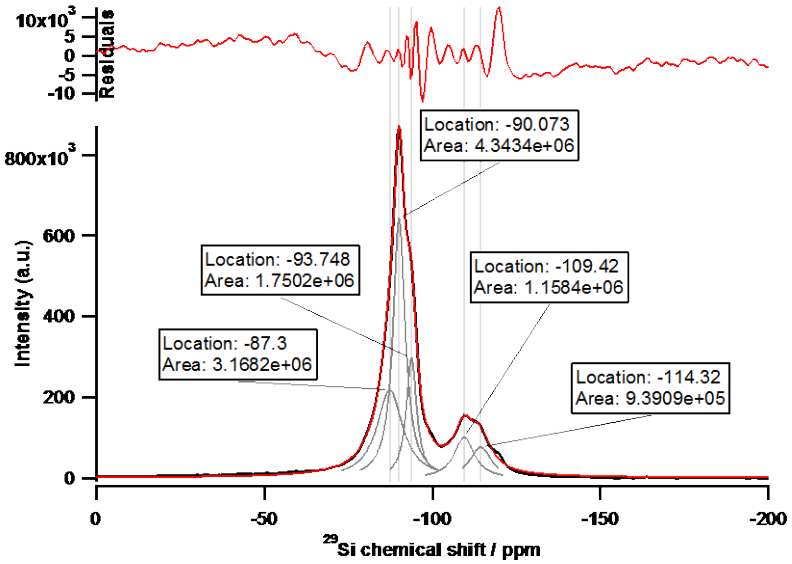

Figure S7. Deconvolution of ^{29}Si direct excitation (DE) solid-state nuclear magnetic resonance (ssNMR) spectrum of enriched high Si SAPO-34 (sample 3).

Table S1. Parameters for the deconvolution of ^{29}Si direct excitation (DE) solid-state nuclear magnetic resonance (ssNMR) spectrum of enriched high Si SAPO-34 (sample 3).

Coordination	Peak	Area	% of area
$Si(OSi)_4$	-114.3, -109.4	2.10E+06	18.5%
$Si(OAl)_3(OSi)$	-93.7	1.75E+06	15.4%
$Si(OAl)_4$	-90.1, -87.3	7.51E+06	66.1%

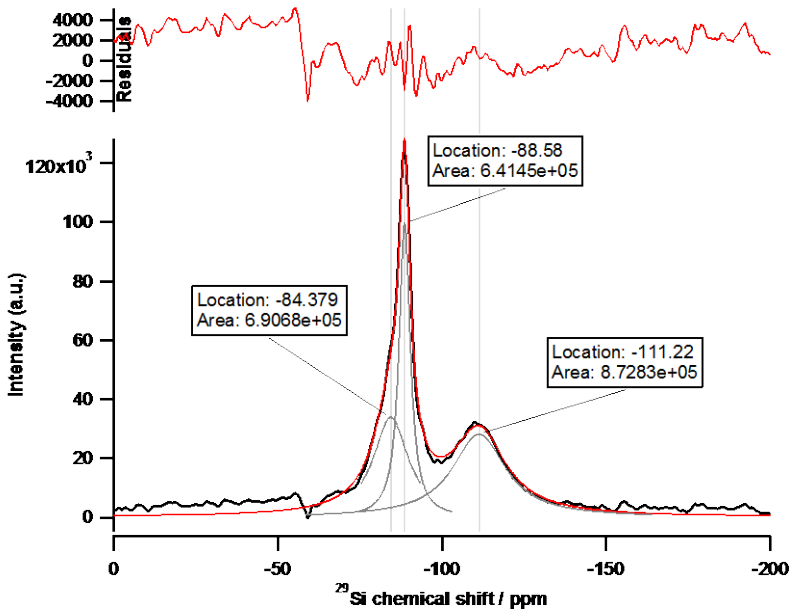

Figure S8. Deconvolution of ^{29}Si direct excitation (DE) solid-state nuclear magnetic resonance (ssNMR) spectrum of enriched low Si SAPO-34 (sample 4).

Table S2. Parameters for the deconvolution of ^{29}Si direct excitation (DE) solid-state nuclear magnetic resonance (ssNMR) spectrum of enriched low Si SAPO-34 (sample 4).

Coordination	Peak	Area	% of area
$Si(OSi)_4$	-111.22	8.37E+05	44.8%
$Si(OAl)_4$	-88.6,-84.4	1.03E+06	55.2%

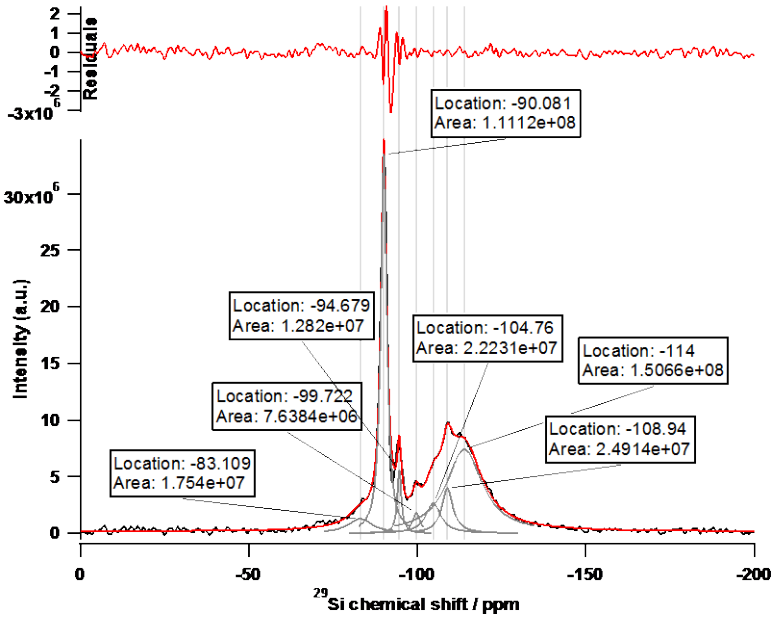

Figure S9. Deconvolution of ^{29}Si direct excitation (DE) solid-state nuclear magnetic resonance (ssNMR) spectrum of large crystals of SAPO-34 (sample 5).

Table S3. Parameters for the deconvolution of ^{29}Si direct excitation (DE) solid-state nuclear magnetic resonance (ssNMR) spectrum of large crystals of SAPO-34 (sample 5).

Coordination	Peak (ppm)	Area	% of area
$Si(OSi)_4$	-114, -109.0	1.756E+08	53.3%
$Si(OAl)(OSi)_3$	-104.8	2.2231E+07	6.7%
$Si(OAl)_2(OSi)_2$	-99.7	7.638E+06	2.3%
$Si(OAl)_3(OSi)$	-95	1.282E+07	3.9%
$Si(OAl)_4$	-90.1	1.1112E+08	33.7%

7. Atom Probe Tomography (APT)

APT was performed using a LEAP 4000X HR local electrode atom probe equipped with laser pulsing capabilities and an energy compensating reflectron lens located within the center for nanomaterials science (CNMS) at Oak Ridge National Laboratory (ORNL). The specimens were run in laser pulse mode with a laser energy of 200 pJ, base temperature of 40 K, pulse repetition rate of 200 kHz, and a detection rate of 1 atom per 200 pulses. The detector has an efficiency of ~37%. Data analysis is described in Section S8, following our previous publications, and includes a detailed discussion of error analysis.[61–63] Needles were prepared for APT analysis using a standard lift-out and needle preparation were performed using standard specimen preparation techniques utilizing Si micro-tip arrays purchased from CAMECA.[64] The LEAP 5000 XS analyses were run at the Cameca factory (Madison, Wisconsin, USA) with the following parameters: detector efficiency 80%, base temperature 40 K, pulse repetition rate of 125 kHz, 50 pJ laser power and a detection rate of 1 atom per 200 pulses.

Data collection and mass spectral interpretation

In our recent review manuscript, we discuss many of the challenges in accurately interpreting APT MS data for MMs and will not reiterate them here, besides discussing SAPO-34 specific challenges.[63] Representative MS of the 5 samples are shown in Figure S10, and it is apparent that these samples generate a large number of peaks, in a similar fashion to what we reported with ZSM-5.[63] The reason for the large number of peaks is that even the calcined material contains Al, H, O, P, Si and molecular fragments of these elements along with all their isotopes in the MS. The complexity becomes more severe with ^{13}C and its molecular fragments in the $^{13}CH_3OH$ reacted material, and increasingly complex for the template molecular fragments for the as-made material. C, N, O and H add a significant amount of complexity in the MS because these ions tend to field evaporate as complex molecular species. Having a diverse range of samples: as-made, calcined, $^{13}CH_3OH$ reacted, and two ^{29}Si enriched samples, allowed us to assign the MS peaks with confidence because we could analyze the changes in the MS when different elements and isotopes were present. Representative MS from the SAPO-34 samples are shown in Figure S10. It is apparent from this figure that many mass species exist, particularly for the template containing material, with some unable to be identified with confidence, but these species only accounted for a small number of the total ions as the counts are in log scale. The importance of the isotopic enrichment for properly interpreting the MS cannot be understated as it allowed us to distinguish between several key, overlapping peaks, as can be seen in Figure S10, which is very important for accurate quantification of APT data.

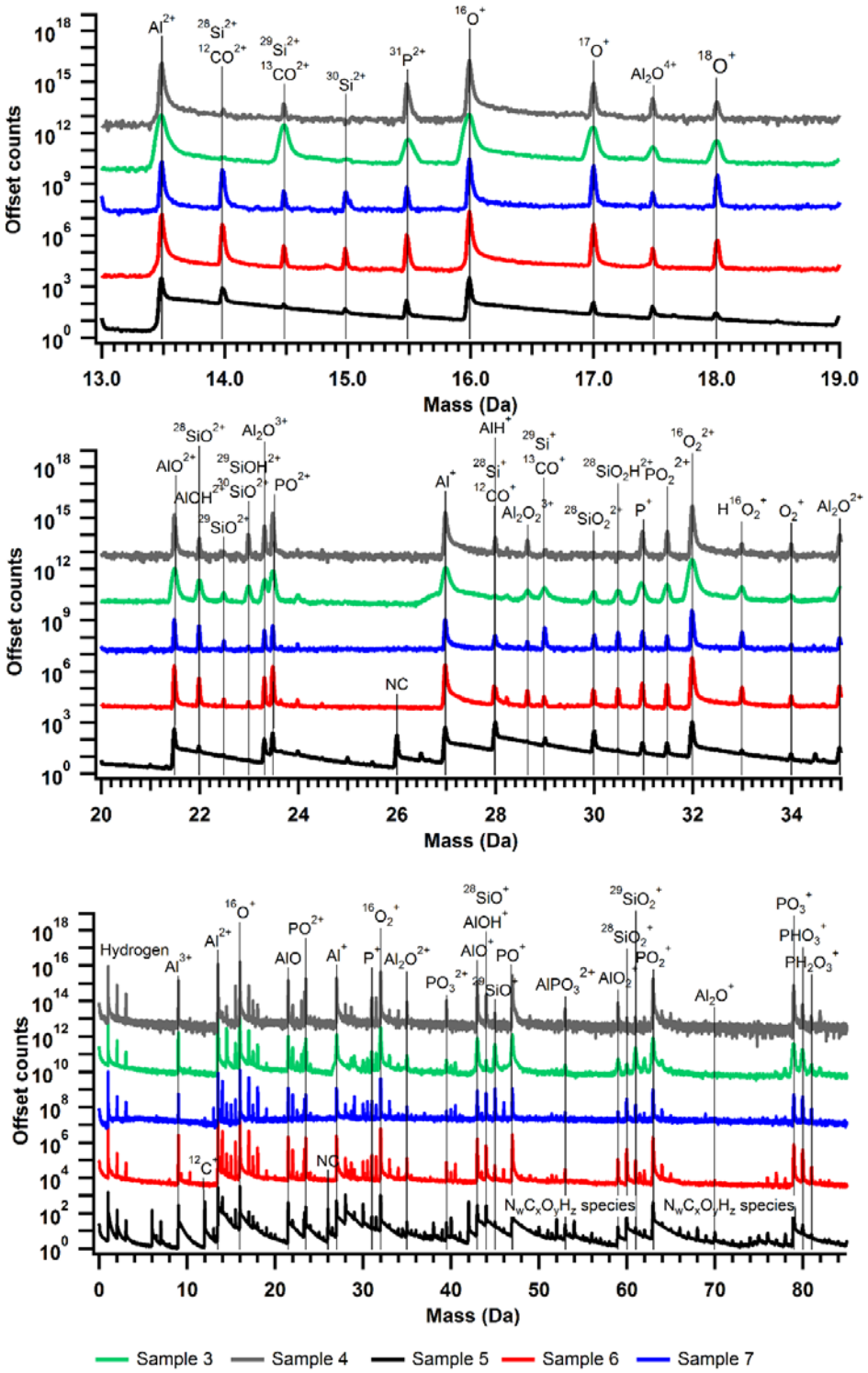

Figure S10. Representative log-scale mass spectra (MS) from atom probe tomography (APT) experiments, with ions of interest indicated and 0.01 Da bin widths. The two upper images are expanded regions with many species.

8. Atom Probe Tomography (APT) Data Analysis

All error analyses were calculated from counting statistics using the method described in reference [65]. In all subsequent discussions, consistent with the terminology used in APT work, 'bulk' refers to the entire needle, 'matrix' refers to the atoms that remain after clusters are removed, and solute refers to the element(s) of interest in cluster analysis. See reference [66] for further details and definitions. In all APT analyses, a small amount of gallium was found to be present due to the FIB-cutting process, and our treatment of this potential influence is discussed in the subsection "Assessing Ga damage." All compositional percentages referred to in this work are atomic percentages. The nonconductive nature of the materials used in this study complicates the data collection. The pulsed laser heating helps to overcome these difficulties. Sample heating creates issues with processing the sample mass spectra as it creates thermal tails in the data. Due to this issue, not all collected data sets gave reliable, quantitative results, and only data sets that gave reliable results are presented. It is known that there are difficulties in quantitatively detecting oxygen or oxides as these tend to field evaporate as double detector hits, which will be registered as a single hit, and there is also evidence that molecular ions can dissociate after field evaporation, such that one ion becomes deionized and does not hit the detector within the appropriate time-of-flight window and is registered as background (even though we attempted to keep the detection rate low, 1 ion per 200 pulses).[61,66,67] These issues can cause deviations from the actual composition, and hard to control experimental parameters can influence the severity of these artefacts. The Local Range-Assisted background estimate embedded in IVAS was used, which estimates the background based on the number of counts before and after the ranged peak.

Isoconcentration surface analysis

Isoconcentration surface analysis is extensively discussed in reference [66] and the references contained therein. The isoconcentration surface analysis is initiated by creating a 3-D grid in concentration space. After this grid is created, 3-D surfaces connecting points of equal elemental concentration can be generated, so called isoconcentration surfaces. These surfaces allow internal features to be identified, and may be defined by a single element or multiple elements. The 3-D grid is created by defining a voxel size and delocalization, with the tradeoff that smaller voxels will give a higher spatial resolution but a greater amount of noise. Once the 3-D grids are generated, relevant isoconcentration surfaces can be found using concentration thresholds. The importance of the isoconcentration surface analysis comes in evaluating the resulting proximity histograms, which allow the border between concentration regions to be quantitatively evaluated. The exact boundary value chosen is not important as it can change with voxel size and delocalization, what is important is that the proximity histograms allow regions that are poor or rich in specific ion(s) to be identified and separated. We generally used the default settings in IVAS ($3 \times 3 \times 3$ nm delocalization and 1 nm voxel size). However, there were instances in which the voxel size was reduced to create a higher polygon density to increase the signal to noise ratio because the edge polygons are not included in the proximity histogram analysis. The delocalization remained the same, so the shape of the interfaces was not significantly altered with the reduced voxel size.

Radial distribution function

The radial distribution function (RDF) is a powerful tool to examine affinity between small numbers of atoms and test homogeneity, and it was applied using CAMECA's IVAS software. The method is extensively discussed in references [68] and [69]. The RDF is conducted by normalizing the local concentration of a selected ion by the bulk concentration, and this is done radially outward from the center of the ion(s) of interest. Error analyses were conducted using counting statistics; because few ions will be counted near each ion of interest, the error bars are high for the first few data points. As the RDF is shown as a bulk normalized concentration, values between pairs of atoms will not be equal. The number of counts is equal for both pairs, but not the bulk normalized concentrations since they are defined over different volumes.

Cluster analysis (maximum separation method)

The purpose of cluster analysis is to identify regions where the spacing between solute atoms in APT data is smaller than that in the bulk, effectively determining regions that are locally enriched in a specified element. For a detailed discussion of the procedure the reader is referred to reference [66]. As a summary, cluster analysis is initialized by choosing a N_{min} value, which is the minimum number of solute atoms that can form a cluster. With N_{min} set, different values of D_{max} can be evaluated. D_{max} defines the maximum distance in which another solute atom must be found to form a cluster (one additional solute atom must be found for order = 1, higher orders are also possible with more than one solute atom required to fall within D_{max}). A minimum value of D_{max} is established such that clusters containing at least N_{min} atoms are identified. There are additional parameters that are used in the analysis, and matrix atoms contained in the cluster can also be identified. The key element of cluster analysis is how the parameters are determined and significant clustering is identified. The significance test is accomplished by first taking the number of solute atoms and volume being considered, and randomizing their position using a normal distribution in space. Then, the same cluster analysis is carried out on the randomized data. Once these two data sets are established, the cluster parameters are determined using an iterative process where N_{min} is first set and then the cluster count is plotted as a function of D_{max}. If the solute data is found to be significantly separated from the randomized data (normally chosen as a point where clusters exist in the collected data and zero, or a very minimal amount, such that >95% of the clusters would be non-random, exist in the randomized data), then D_{max} can be fixed. A fixed D_{max} can then be used to plot cluster count versus cluster size to set an optimal N_{min}. By iterating through these parameters, the optimal cluster D_{max} and N_{min} can be determined, where significant clusters can be found relative to the randomized data. This iterative process as applied through the cluster count distribution (CCD) and cluster size distribution (CSD) as applied to the data sets in this manuscript are shown with the analyses for each individual parameter along with the other parameters determined for each specific cluster analysis.

A simple method that is useful in identifying if clusters are present and a cluster analysis should be initiated, is by directly comparing the nearest neighbor distributions (NNDs) of the solute and randomized data.[70] In doing this, the number of counts is plotted as a function of the

atom pair distance. For the randomized data this will, by definition, give a normal distribution. However, if clustering is present, then the solute NNDs will be shifted to a smaller atom pair distance. The NND for the solute data is then described best by at least two Gaussians, one centered at a smaller atom pair distance, representing the clusters, and a second centered at an atom pair distance greater than the normal distribution of the randomized data, representing the matrix ion spacing. This makes plotting the NNDs an invaluable tool in cluster analysis.

Assessing Ga damage

It is well known in APT that Ga damage can be problematic as it may influence the position of ions, making any findings the result of needle fabrication rather than an actual material property, potentially leading to incorrect conclusions. In order to minimize this during zeolite sample preparation, we coated the samples with Pt using FIB deposition. A 30 kV beam was used for the initial milling, leaving an ~250 nm wide needle with several hundred nm's of Pt remaining on the surface. A 2 kV final milling step was used to remove the Pt cap. The zeolite material mills much faster than the Pt cap, and therefore, the tip shape was finally a very sharp needle with a shank angle. We were also careful to minimize the ebeam exposure to the material because zeolites also suffer from damage resulting from the ebeam. Potential Ga damage has been an issue that we were also concerned with when analyzing the data, so we used a Ga isoconcentration surface to remove the Ga rich portions of the needle (normally the needle tip and surface) prior to any analyses by exporting the low gradient side of a Ga interface. The figures show the full datasets for aesthetic purposes.

APT data analysis workflow

The processing and analysis of the data obtained in an APT experiment is far from trivial and is the subject of active research and debate.[66,71–73] Below is a brief outline of the normal workflow used in the processing of APT data as performed for the experiments described herein. This is not meant to be an exhaustive or definitive guide, but rather a brief overview in order to give the reader an idea of the process used, and the reader is referred to our previous manuscript for further details.[61]

1. Data collection with an APT instrument.
2. Data processing and reconstruction: When processing zeolite samples it is especially important that all peaks are ranged correctly. The 3-D distribution of all ions can then be generated.
3. Determining if there exists segregation of elements: Nearest neighbor distributions (NNDs), frequency distribution analysis (FDA) and radial distribution functions (RDFs) are used to examine compositional heterogeneities.
4. Identification of isoconcentration surfaces: Isoconcentration surface analysis is used to separate large compositional heterogeneities. The isoconcentration surfaces are quantified using proximity histograms.
5. Cluster analysis: The identification of clusters is an iterative process between comparing the cluster count distribution (CCD) and cluster size distribution (CSD) after determining a starting d_{max} using the NND. Therefore, statistically relevant clusters can be identified.

Error analysis

Error analyses in APT are based on counting statistics, and the method as applied to APT is discussed in references [65,74,75]. From counting statistics, the standard error in the concentration of species *X*, defined as $C_X = \frac{n_X}{n_t}$, can be calculated as $s_X = \sqrt{\frac{c_X(1-c_X)}{n_t}}$. This standard error defines a 95% confidence interval or a 2σ threshold by the conventional definition. This allows the error in concentration to readily be determined. Because of the method used for error determination, when only small numbers of an ion of interest are detected the error will be large. This is evident in the RDF plots where the error bars at small distances from the species of interest are large due to the small number of counts. In order to calculate the propagation of error for atomic ratios, the general variance formula was used.[76]

$$\sigma_f = \sqrt{\left(\frac{\partial f}{\partial x}\right)^2 \sigma_x^2 + \left(\frac{\partial f}{\partial y}\right)^2 \sigma_y^2 + \left(\frac{\partial f}{\partial z}\right)^2 \sigma_z^2 + \cdots}$$

Where σ_f represents the standard deviation of the function f, σ_x represents the standard deviation of x, etc.

Applied to $\frac{Si}{Si+Al+P}$, which is equivalent to $\frac{C_{Si}}{C_{Si}+C_{Al}+C_P}$, but concentrations will be used as the error from counting statistics is for the concentration. Similar error propagation formulas can also be derived for Al and P.

$$\sigma_{\frac{Si}{Si+Al+P}} = \sigma_{\frac{C_{Si}}{C_{Si}+C_{Al}+C_P}} = \sqrt{\left(\frac{\partial\left(\frac{C_{Si}}{C_{Si}+C_{Al}+C_P}\right)}{\partial C_{Si}}\right)^2 \sigma_{C_{Si}}^2 + \left(\frac{\partial\left(\frac{C_{Si}}{C_{Si}+C_{Al}+C_P}\right)}{\partial C_{Al}}\right)^2 \sigma_{C_{Al}}^2 + \left(\frac{\partial\left(\frac{C_{Si}}{C_{Si}+C_{Al}+C_P}\right)}{\partial C_P}\right)^2 \sigma_P^2}$$

Where

$$\frac{\partial\left(\frac{C_{Si}}{C_{Si}+C_{Al}+C_P}\right)}{\partial C_{Si}} = \frac{C_{Al}+C_P}{(C_{Si}+C_{Al}+C_P)^2}$$

$$\frac{\partial\left(\frac{C_{Si}}{C_{Si}+C_{Al}+C_P}\right)}{\partial C_{Al}} = -\frac{C_{Si}}{(C_{Si}+C_{Al}+C_P)^2}$$

$$\frac{\partial\left(\frac{C_{Si}}{C_{Si}+C_{Al}+C_P}\right)}{\partial C_P} = -\frac{C_{Si}}{(C_{Si}+C_{Al}+C_P)^2}$$

9. Needle Compositions

During the course of this project 36 atom probe data sets were collected, and of those 22 produced reliable and useable data, *i.e.* the collection of a significant number of ions prior to needle failure and high MS quality.[63] Table S4 presents the compositions of the 22 different needles. Examining this table reveals several important features about the materials and the ability to quantify the elements present. In the samples made with enriched ^{29}Si (needles 1 to 5), the Si contents are fairly uniform within all samples, and there is a significant difference in composition between the high and low Si materials, as expected. In the template containing large crystals of SAPO-34 (needles 6-11) the ^{12}C/N ratio ranges from ~2-3, which is lower than the stoichiometric value expected for morpholine(C/N=4), however the difficulties in quantifying complex organic molecules were already discussed, and the MS in Figure S10 reveals the abundance of organic peaks, making the analysis difficult, especially as ^{12}C, ^{14}N and ^{16}O only vary by 2 Da, so they could easily be confused with H present as part of any ion, and certain peaks could be identified with varying combinations of the 3 elements. For the rest of the needles, the ratios of Al, P and Si are consistent, except for some of the $^{13}CH_3OH$ reacted materials that have a higher Si content. This may be due to either overlapping peaks of coke species with framework elements or preparing APT needles from areas within the crystal with slightly higher Si contents.

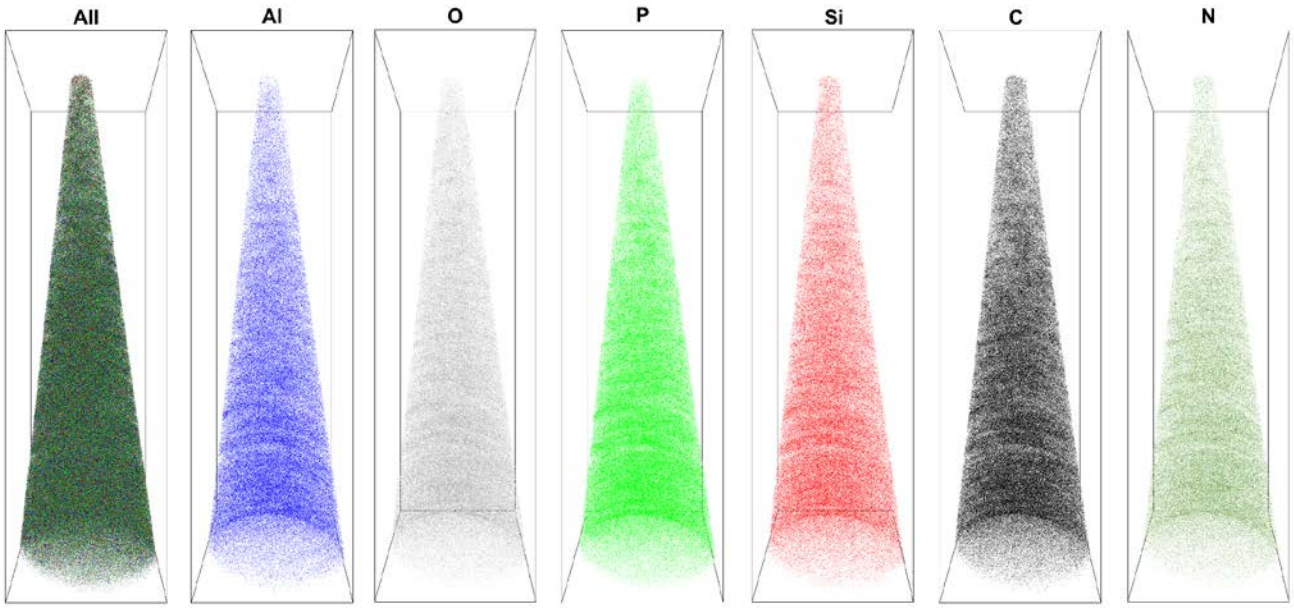

Figure S11. Reconstruction of a representative SAPO-34 needle (needle 8). Bounding box dimensions 281 × 79 × 78 nm^3. These images are also included as Movie S2.

Table S4. Compositions of all APT needles as well as total number of ions collected and ratios of the tetrahedral atoms (Al, P, Si). The notation (S#) following the needle number indicates the sample number the needle was taken from.

	1 (S3)	2 (S3)	3 (S3)	4 (S4)	5 (S3)	6 (S5)	7 (S5)	8 (S5)
Al	19.6%	20.0%	20.9%	19.1%	19.6%	16.1%	16.0%	16.8%
O	62.4%	62.1%	61.8%	63.0%	62.2%	53.1%	53.7%	54.0%
Si	5.0%	5.4%	5.1%	0.2%	0.1%	2.1%	2.3%	2.4%
P	12.9%	12.6%	12.2%	17.7%	18.1%	11.3%	9.8%	11.4%
^{12}C						11.5%	12.5%	9.3%
N						5.9%	5.7%	6.2%
^{13}C								
Total Ions	4,604,424	4,989,301	1,125,870	758,812	935,805	21,718,149	3,557,736	5,631,896
Si/(Si+Al+P)	0.13	0.14	0.13	0.0048	0.0018	0.07	0.08	0.08
Al/(Si+Al+P)	0.52	0.53	0.55	0.52	0.52	0.50	0.57	0.55
P/(Si+Al+P)	0.34	0.33	0.32	0.48	0.48	0.43	0.35	0.37

	9 (S5)	10 (S5)	11 (S5)	12 (S6)	13 (S6)	14 (S6)	15 (S6)	16 (S6)
Al	14.3%	12.2%	15.3%	18.8%	18.6%	17.6%	17.7%	17.9%
O	54.0%	56.5%	55.2%	61.9%	62.1%	63.6%	63.0%	62.9%
Si	2.2%	1.7%	2.1%	5.3%	5.4%	4.8%	5.0%	5.1%
P	8.8%	10.3%	9.2%	14.0%	13.8%	13.9%	14.2%	14.1%
^{12}C	15.1%	13.5%	12.6%					
N	5.5%	5.8%	5.7%					
^{13}C								
Total Ions	1,773,553	1,902,033	3,005,334	9,383,511	1,538,012	5,085,337	5,906,828	2,662,452
Si/(Si+Al+P)	0.09	0.07	0.08	0.14	0.14	0.13	0.13	0.14
Al/(Si+Al+P)	0.56	0.50	0.58	0.49	0.49	0.49	0.48	0.48
P/(Si+Al+P)	0.35	0.43	0.35	0.37	0.37	0.38	0.38	0.38

	17 (S7)	18 (S7)	19 (S7)	20 (S7)	21 (S7)	22 (S7)
Al	17.7%	18.0%	15.4%	14.1%	15.3%	14.9%
O	63.7%	62.3%	64.2%	65.2%	64.2%	64.8%
Si	4.3%	4.7%	5.9%	5.8%	6.2%	6.0%
P	13.8%	13.3%	10.5%	10.8%	11.4%	10.9%
^{12}C	0.2%	0.5%	0.5%	0.5%	0.4%	0.5%
N						
^{13}C	0.2%	1.2%	3.5%	3.5%	2.5%	2.9%
Total Ions	5,890,504	1,565,144	919,844	869,898	1,018,950	786,724
Si/(Si+Al+P)	0.12	0.13	0.19	0.19	0.19	0.19
Al/(Si+Al+P)	0.50	0.50	0.48	0.46	0.47	0.47
P/(Si+Al+P)	0.39	0.37	0.33	0.35	0.35	0.34

10. Si Nearest Neighbor Distributions (NNDs)

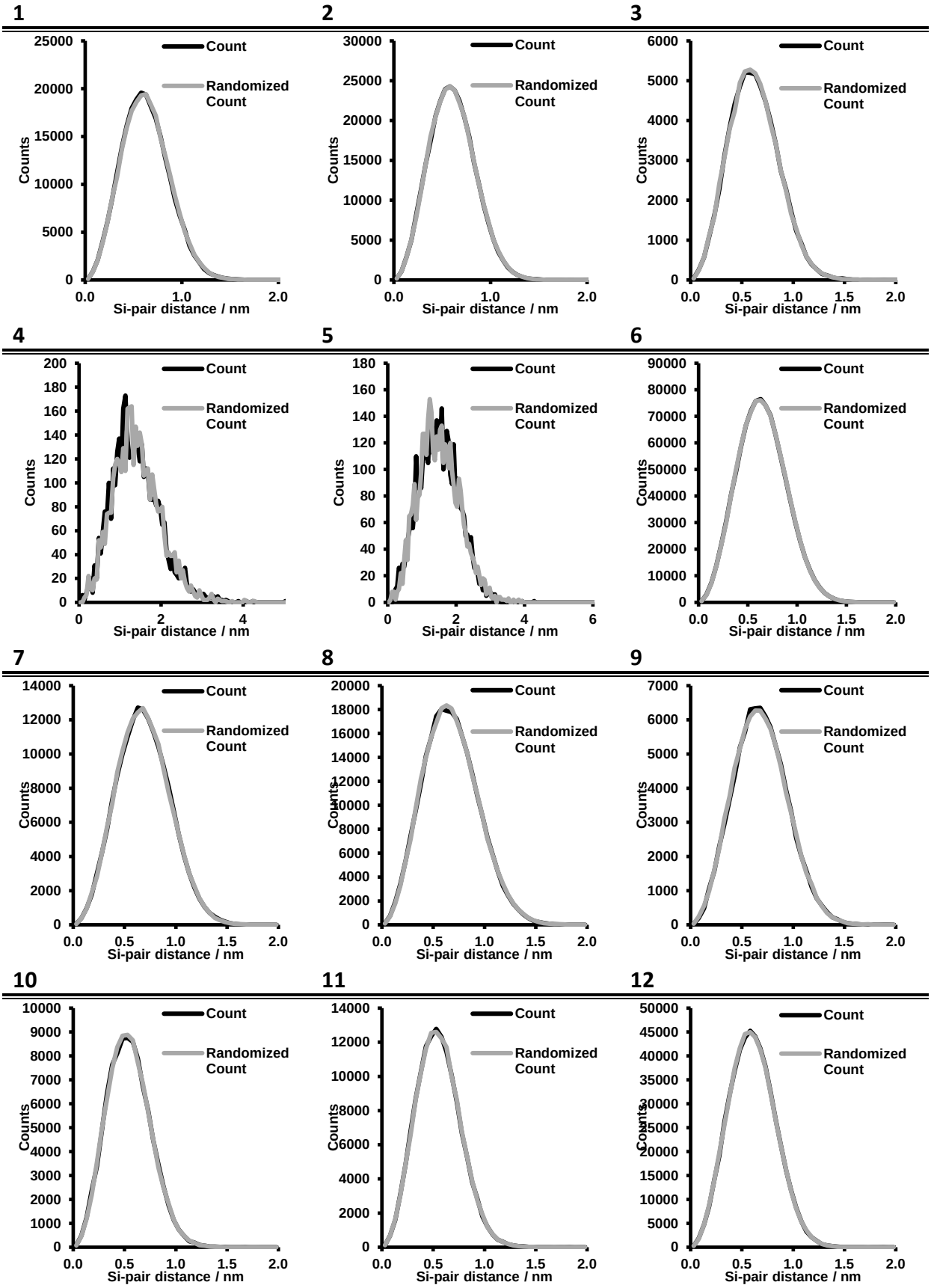

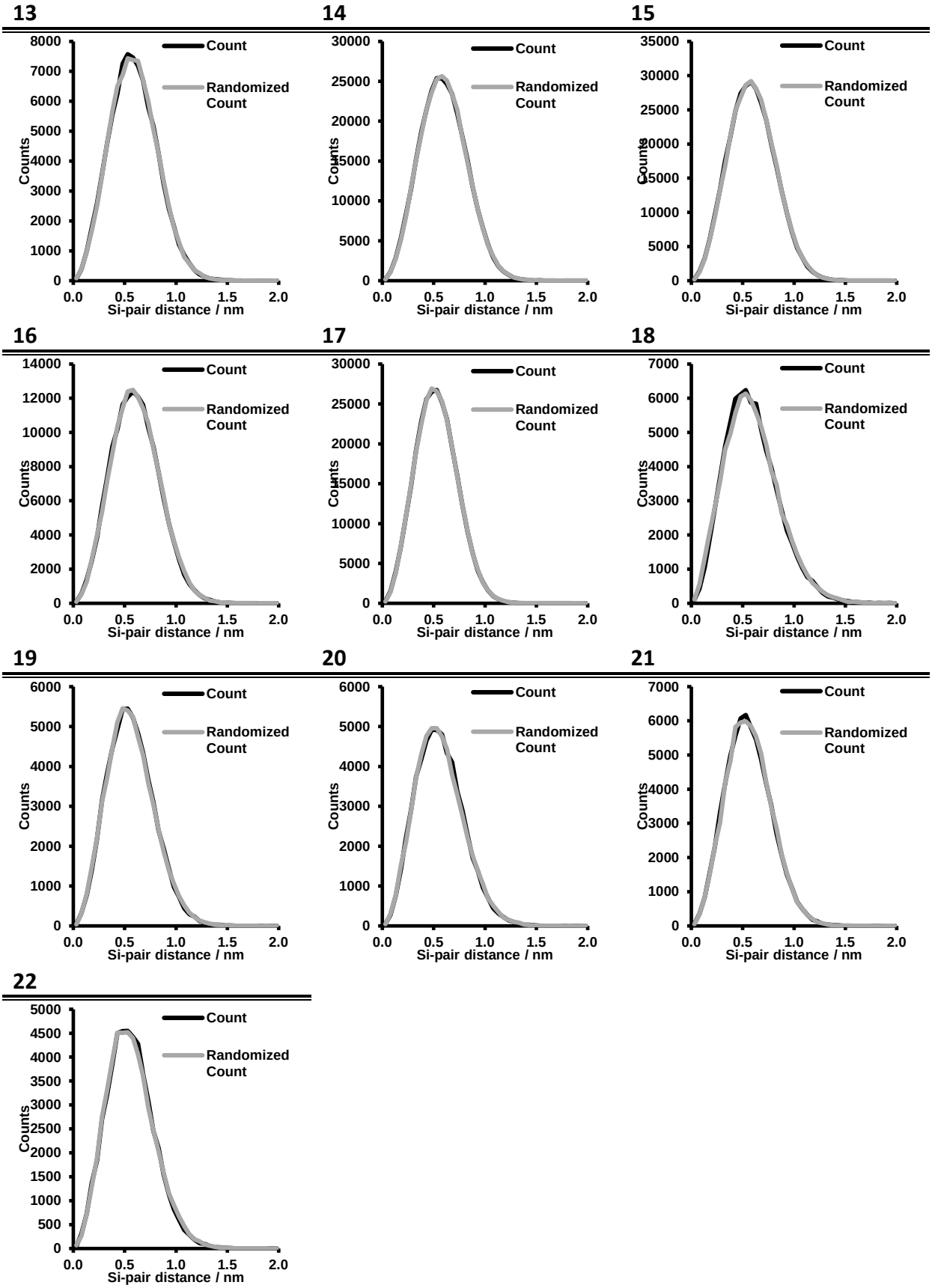

Figure S12. Silicon nearest neighbor distributions (NNDs) for all samples (order =1).

11. Template Nearest Neighbor Distributions (NNDs)

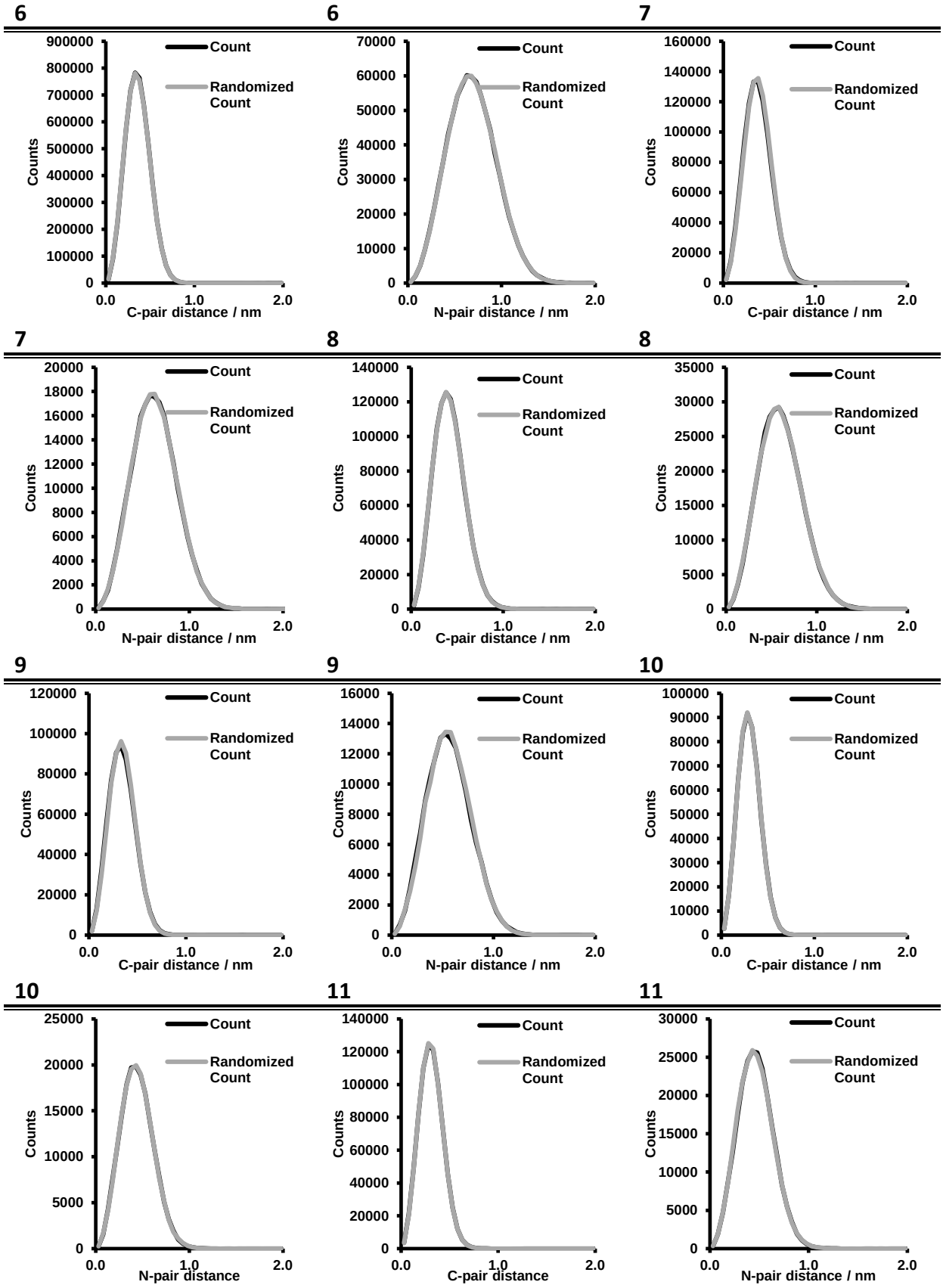

Figure S13. Template (C, N) nearest neighbor distributions (NNDs) for samples 6-11 (order =1).

12. Coke Nearest Neighbor Distributions (NNDs)

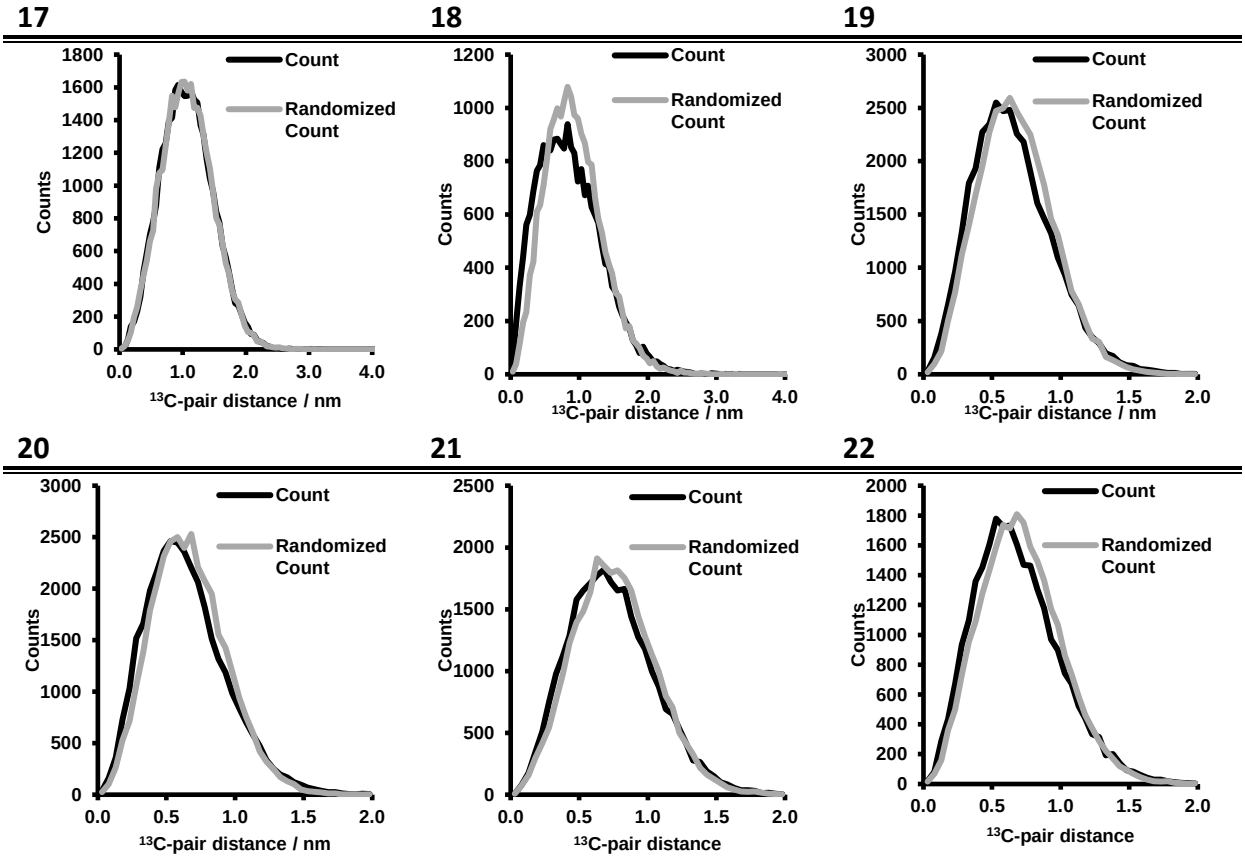

Figure S14. Coke (^{13}C) nearest neighbor distributions (NNDs) for samples 17-22 (order =1).

13. Si Radial Distribution Functions (RDFs)

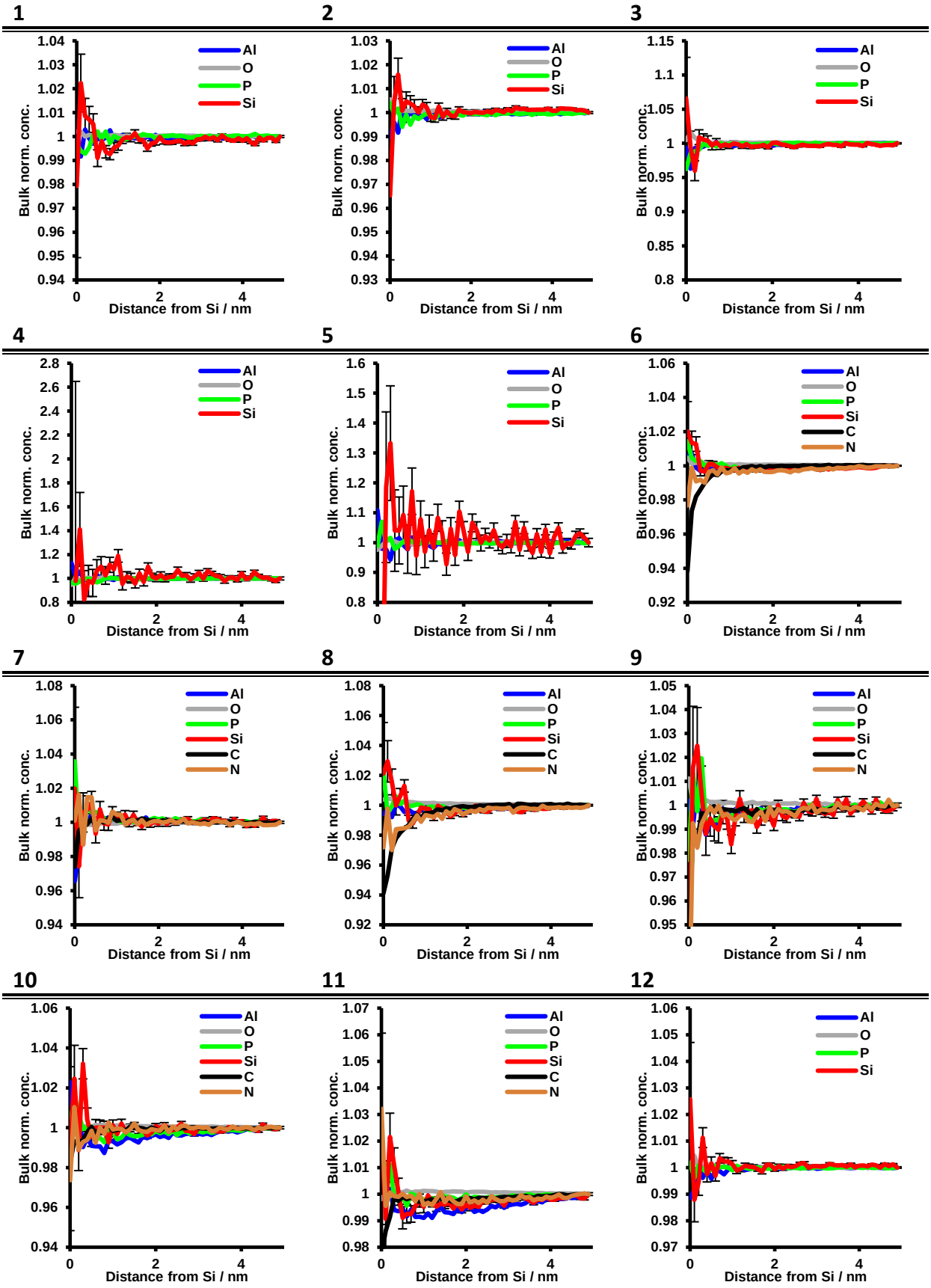

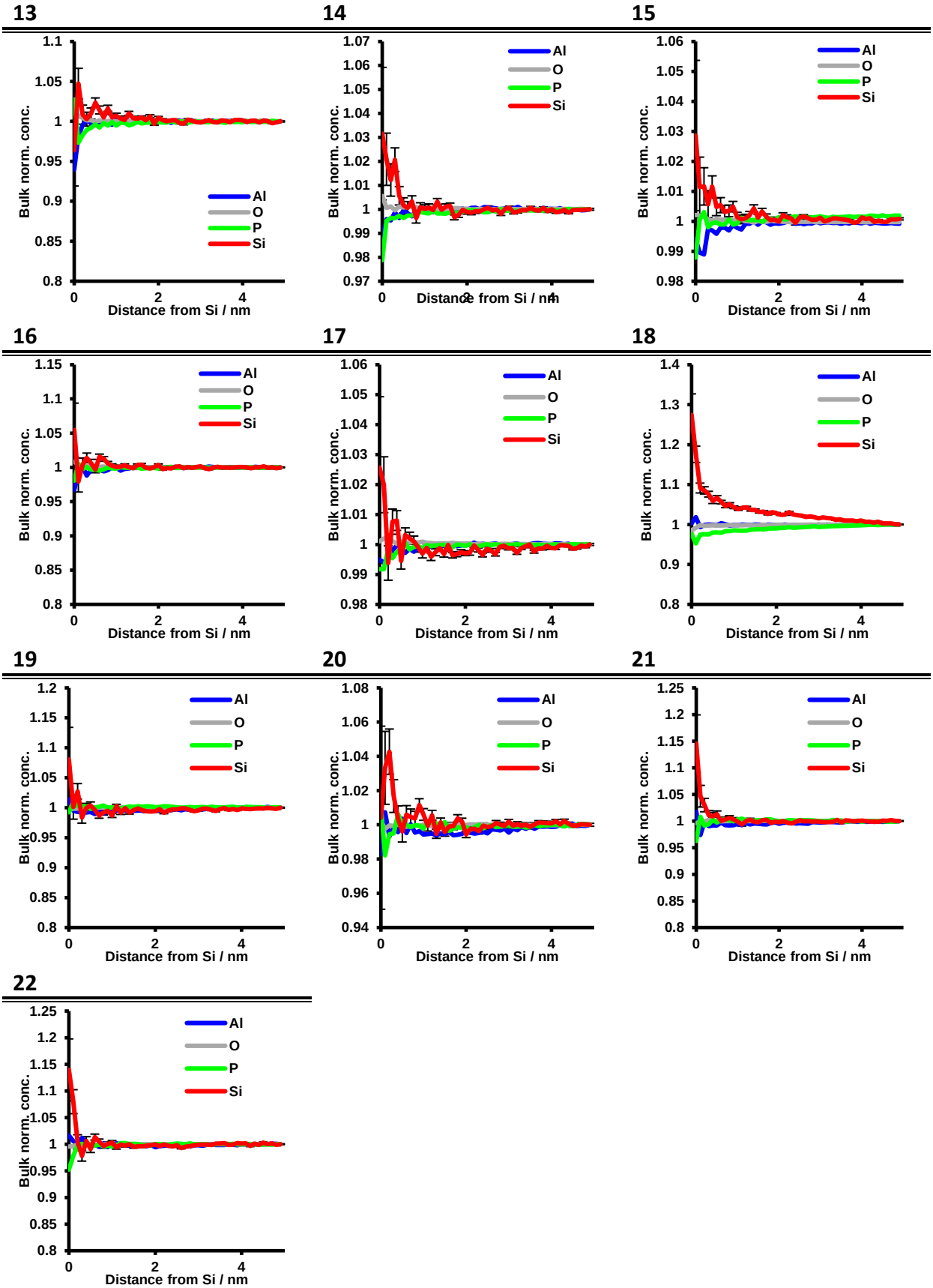

Figure S15. Si radial distribution functions (RDFs) for all samples. In samples 17-22 ^{13}C is not shown as its heterogeneous distribution makes it appear that there is a Si-^{13}C affinity, further discussed in Figure S18.

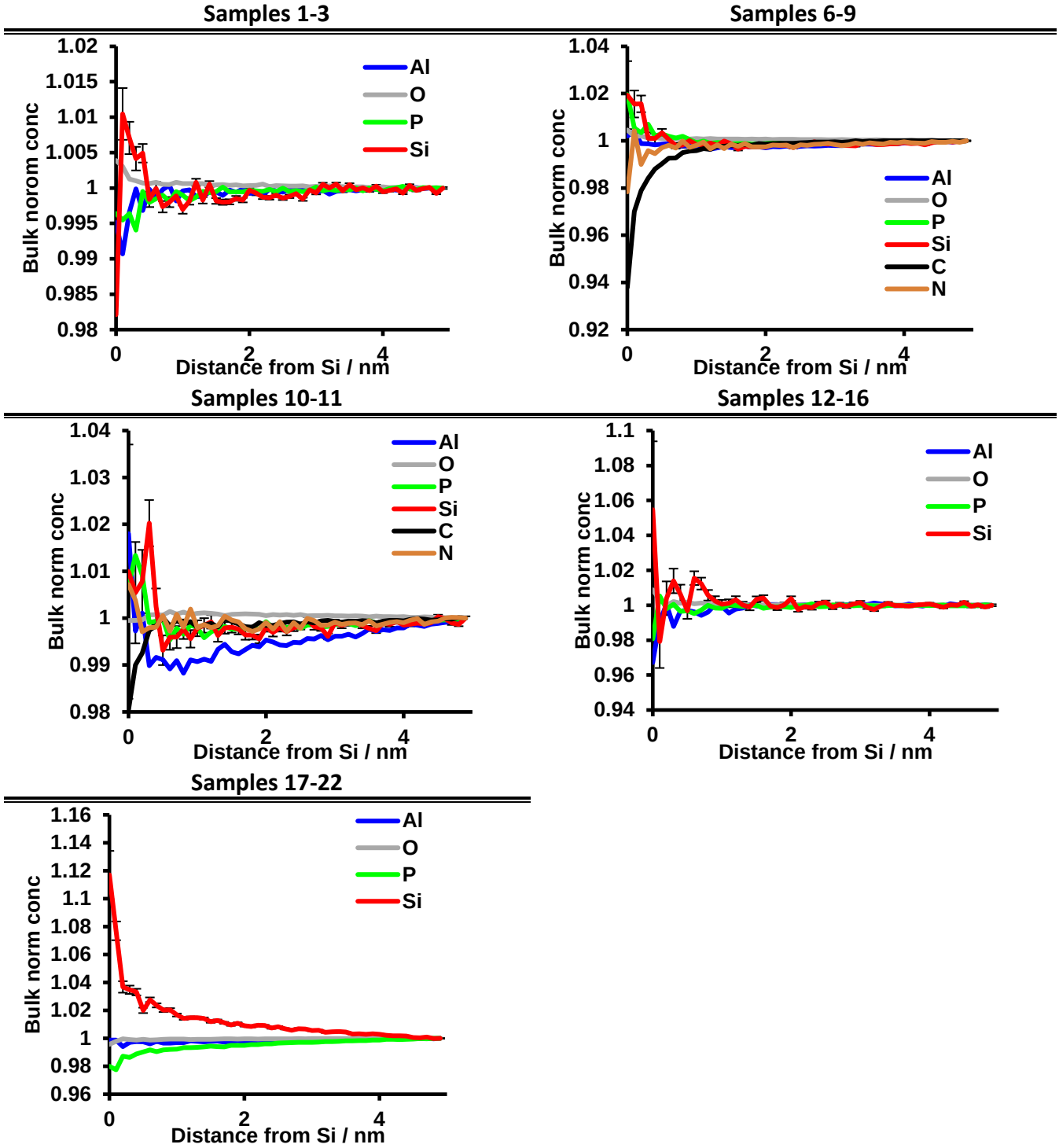

Figure S16. Combined Si radial distribution functions (RDFs) for APT experiments from the same sample. The ^{13}C has been removed from the combined RDFs for the coked materials, samples 17-22, as the heterogeneous ^{13}C distribution skews the result, as is further discussed in Figure S18. The combined RDF for 17-22 shows the strongest Si-Si affinity, and in all the other needles there was a small Si-Si affinity present in the RDFs, though not as strongly as in the coke containing needles. There two strong explanations for this: i) The complexity of the template containing MS increases the probability of $C_wN_xO_yH_z$ peaks to overlap with Si containing peaks. ii) The methanol-to-hydrocarbons (MTH) reaction may lead to Si migration into larger islands, making them easier to detect (note this sample is the same as in needles 6-22, but is MTH reacted after calcination). While it is impossible to determine the exact reason why this sample shows the most significant Si-Si affinity, it is exciting to find this correlation as it is a significant challenge to find atomic-level affinities between light elements.

14. ^{13}C Radial Distribution Functions (RDFs)

17

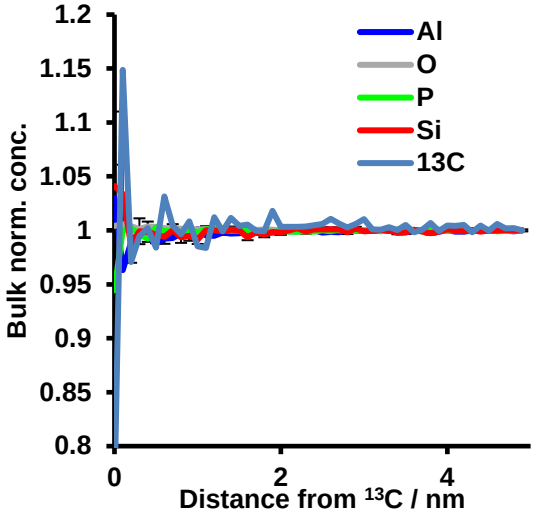

18

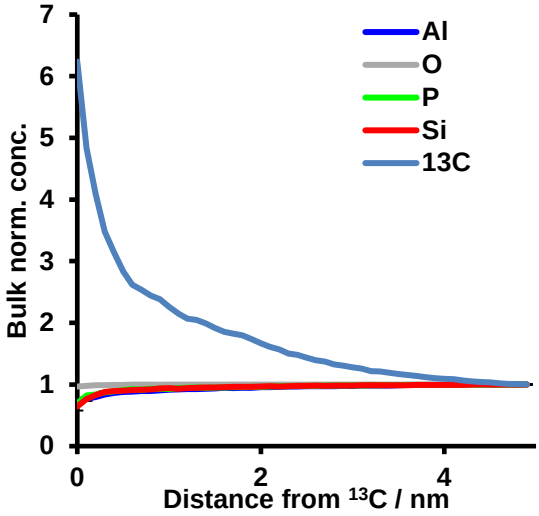

19

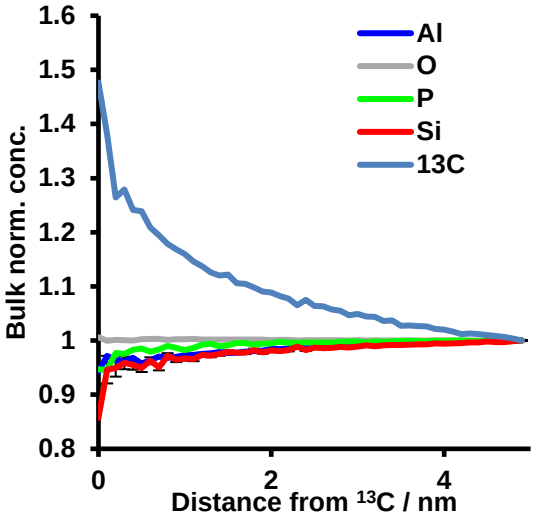

20

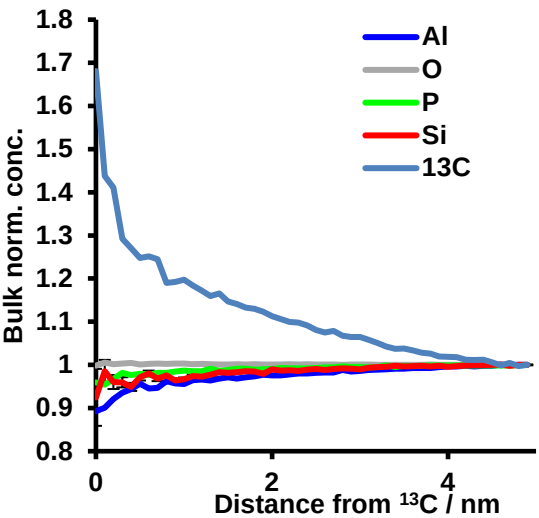

21

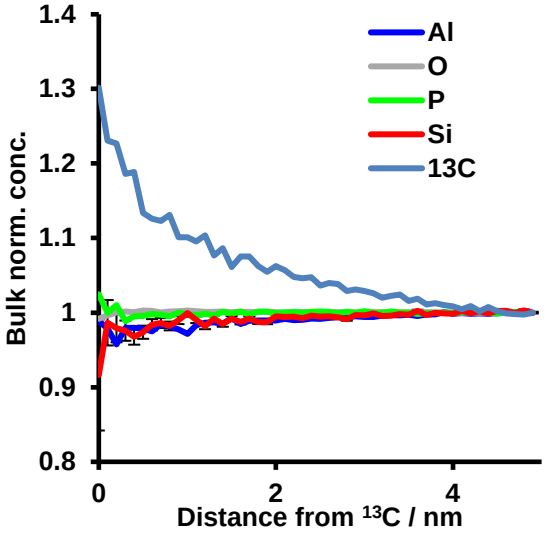

22

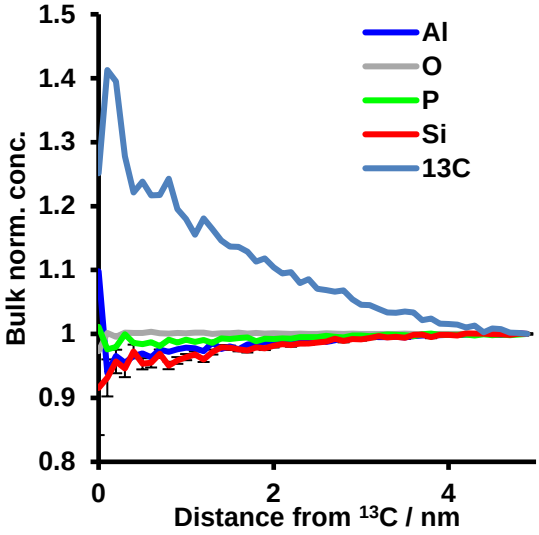

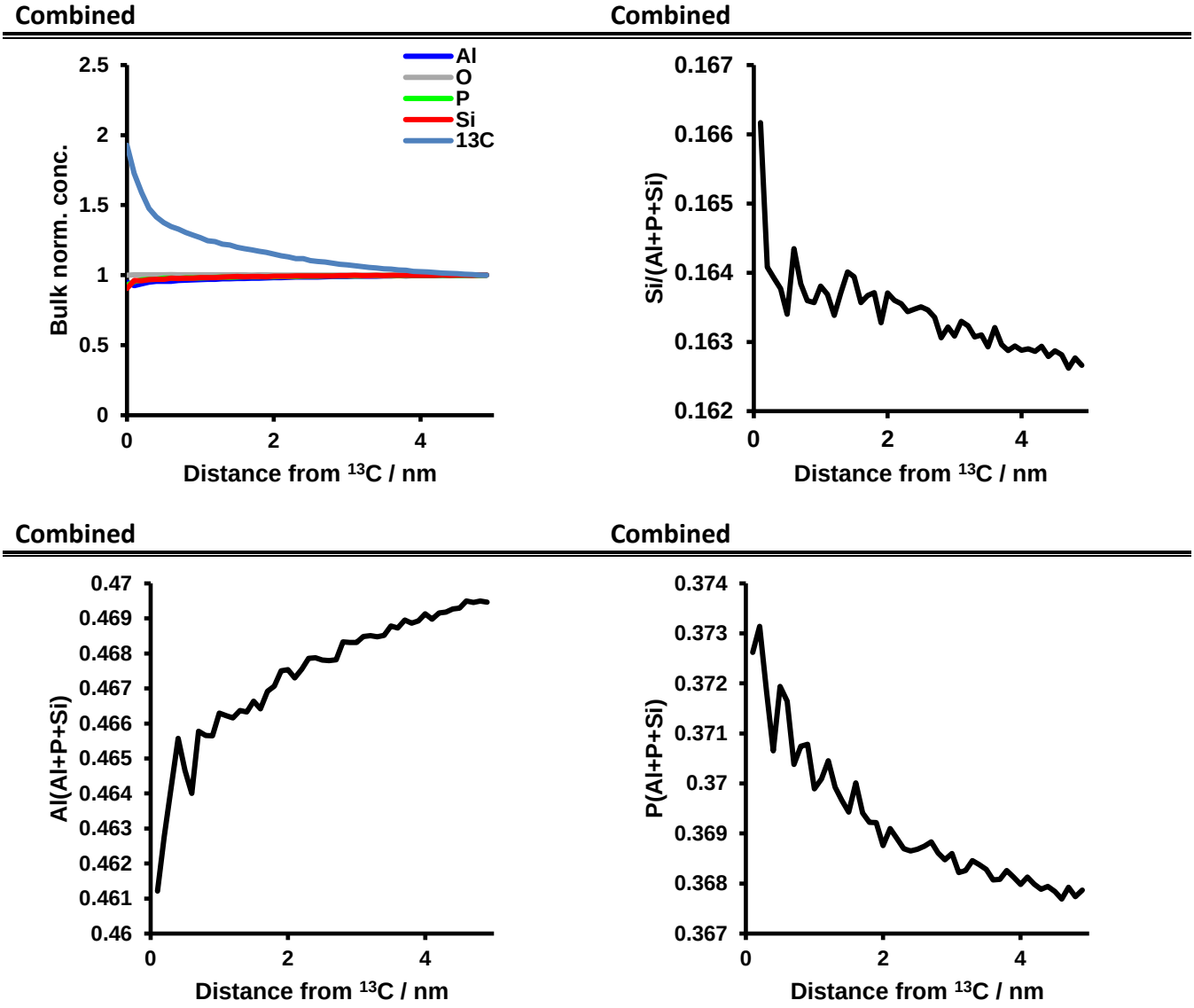

Figure S17. ^{13}C radial distribution functions (RDFs) for samples 17-22 as well as the combined RDF for samples 17-22.

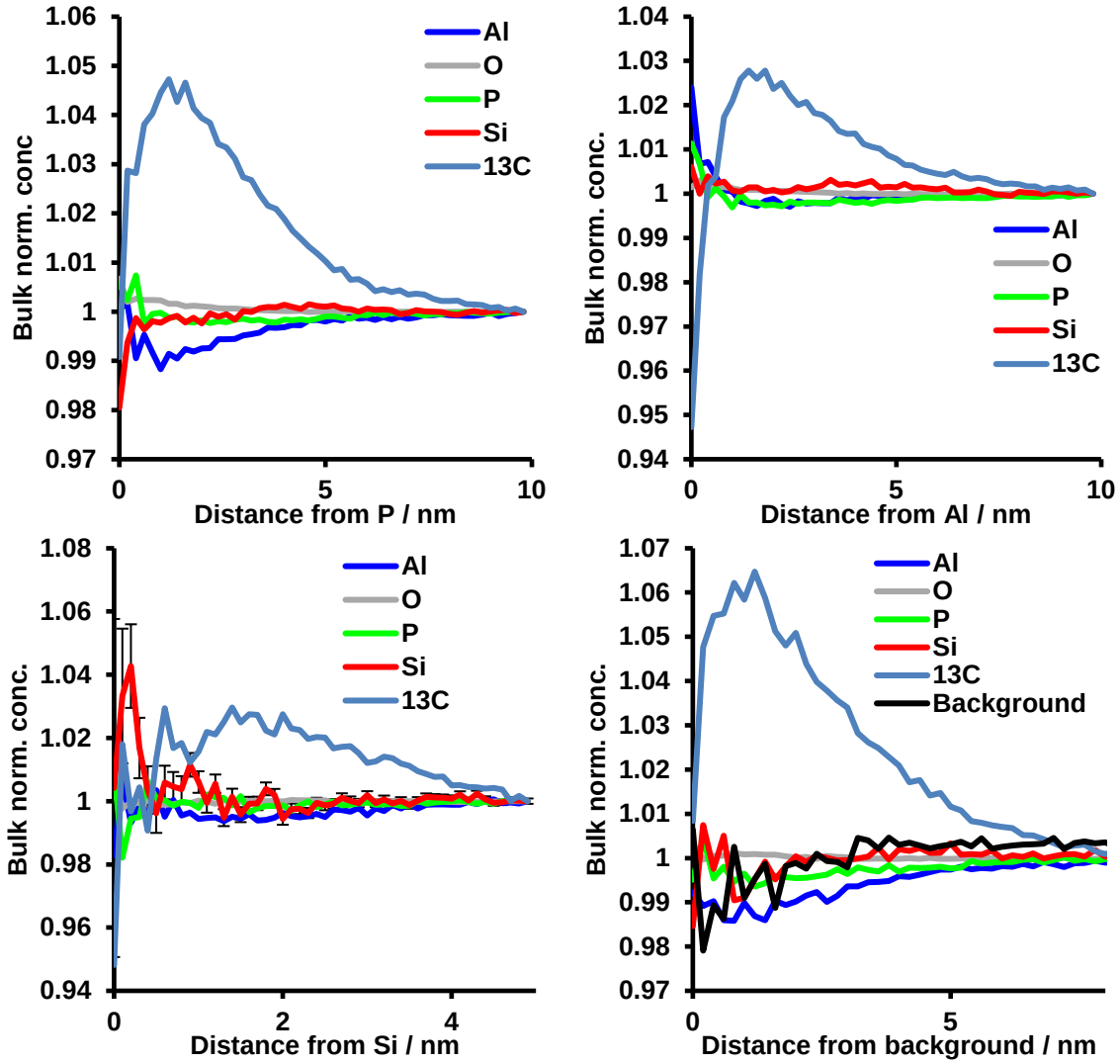

Figure S18. Needle 20 radial distribution functions (RDFs) for Al, P, Si and the background to demonstrate that the heterogeneous ^{13}C distribution can make it appear that there are affinities with ^{13}C that do not really exist. The background centered RDF clearly demonstrates this as it is homogeneously distributed, but still shows an affinity with ^{13}C. Overall, this makes it impossible to determine if a significant Si-^{13}C affinity is present.

15. Template Radial Distribution Functions (RDFs)

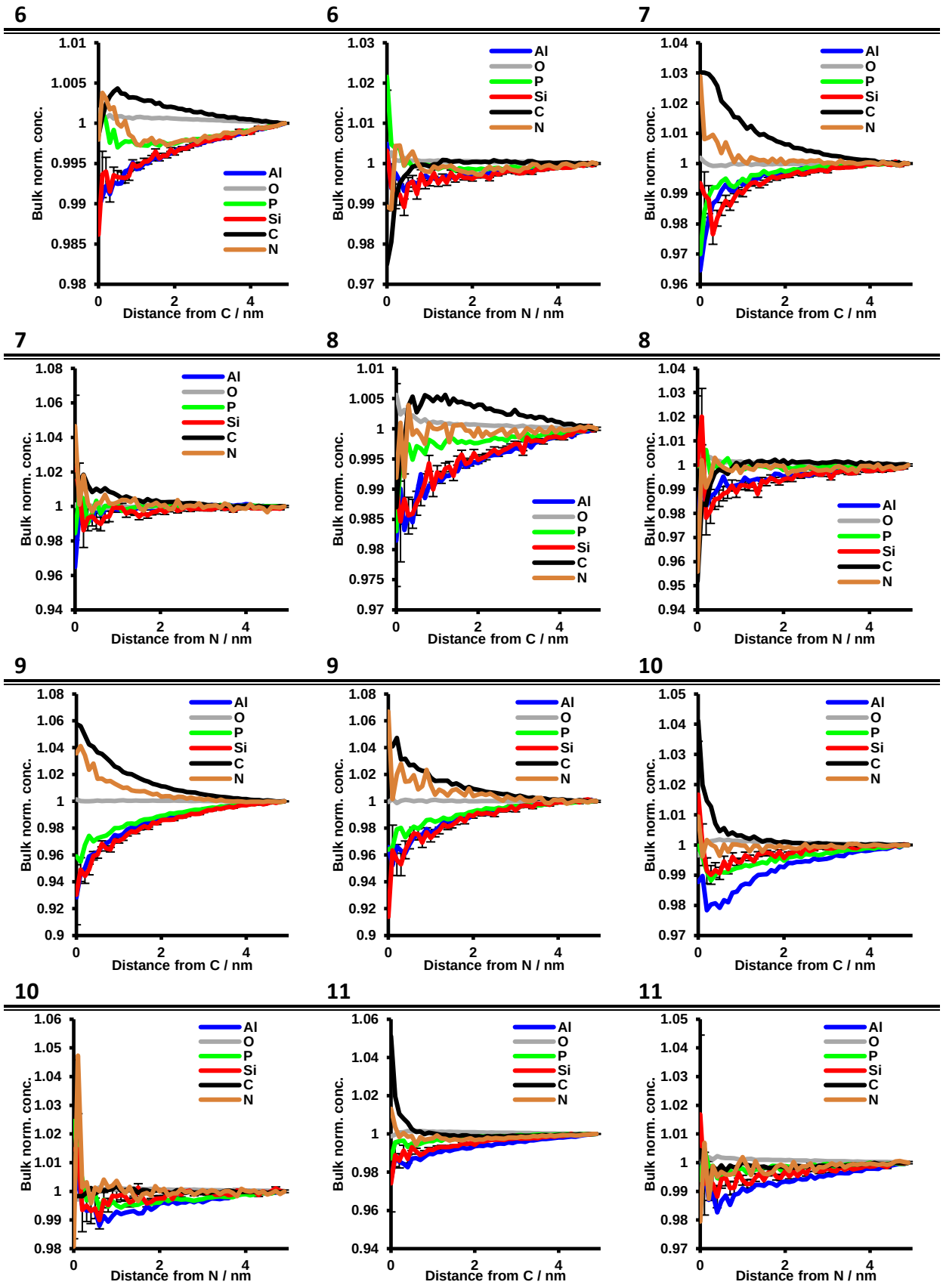

Figure S19. Template element (C, N) radial distribution functions (RDFs) for samples 6-11.

16. Coke Cluster Analysis of Needle 20

Only a few statistically significant ^{13}C clusters were identified (those beyond the amount in a random distribution in the cluster count distribution), with the cluster analysis parameters in Table S5 along with a comparison of the composition of the bulk and clusters in Table S6. Fourteen clusters were identified that range in size from 7-18 ^{13}C atoms (N_{min}=7), with an average size of 8.9 ^{13}C atoms per cluster and a median size of 7 atoms per cluster, making these on average small clusters, close to N_{min} for the analysis. Additionally, within the clusters the Si/(Si+Al+P) ratio is 0.3 while it is 0.2 in the bulk of the needle, illustrating that these coke clusters may form near Si, the Brønsted acid site. Table S6 shows the error analysis for atomic ratios, and the increase in acid site density (Si fraction) within the clusters is beyond the 2σ measurement error (95% confidence interval).

In our cluster analysis of ZSM-5 we were able to identify on the order of 100 clusters per needle (N_{min}=10 for cluster size), while in SAPO-34 we could only identify 14 clusters with N_{min}=7 in one needle. Additionally, in SAPO-34 the largest cluster was only 18 ^{13}C atoms (median size of 7 ^{13}C ions) while in ZSM-5 clusters of hundreds of ^{13}C ions were identified. These differences in the coke clusters are consistent with the material frameworks as the larger pores in ZSM-5 will allow for the formation of large polycyclic coke species, while the small pores and cages in SAPO-34 will not allow such large coke agglomerations to form. These observations are in line with our group's (Utrecht University) previous findings on the significant differences in coking in ZSM-5 and SAPO-34, using primarily UV-Vis (micro-)spectroscopy, to probe different types of coke species present in each material, especially regarding differences in the size of coke molecules between the two frameworks, which in this case can be considered to be indicated by cluster size. [77–80] Additionally, as the coke species in SAPO-34 should only contain around 10 carbon atoms they would be difficult to identify with cluster analysis, by extending the simulation results for Si cluster identification.

Table S5. Custer analysis parameters and cluster sizes for the analysis of coke in needle 20.

Ion(s)	^{13}C	^{13}CO	$^{13}CO_2$
d-max (nm)	0.37		
Order (ions)	1		
N-min (ions)	7		
L (nm)	0.37		
d-erosion (nm)	0.3		
Cluster Count	14		

	Solute Ions	**Ranged Ions**	**Total Ions**
Matrix	33969	561249	1488815
Cluster 1	7	17	24
Cluster 2	7	13	18
Cluster 3	7	16	22
Cluster 4	9	12	22
Cluster 5	7	12	22
Cluster 6	7	10	17
Cluster 7	18	33	52
Cluster 8	13	19	33
Cluster 9	7	9	15
Cluster 10	10	17	25
Cluster 11	10	14	23
Cluster 12	7	10	16
Cluster 13	8	11	23
Cluster 14	7	10	16

Table S6. Bulk versus cluster composition for the ^{13}C clusters extracted from needle 20 along with the atomic ratios of tetrahedral elements and error calculations (error analysis reported below). As the number of counts in the clusters is low the error will be high. The Si content in the clusters is significantly higher than in the matrix (bulk), however this is only a preliminary result and a more comprehensive and dedicated study would be required to reduce the uncertainty in these measurements. The high oxygen content is anticipated as the majority of the ^{13}C was detected as $^{13}CO_2$. The error calculation for the ratio is discussed in Section S8.

	Matrix (bulk)				Cluster		
Ion Type	Count	Atomic %	Error	Ion Type	Count	Atomic %	Error
Al	123094.8	14.15%	0.04%	Al	12.2	2.51%	0.73%
O	564569.8	64.88%	0.11%	O	315.2	64.61%	4.67%
Si	52191.4	6.00%	0.03%	Si	14.4	2.95%	0.79%
P	93773.7	10.78%	0.04%	P	16.0	3.29%	0.83%
^{13}C	30398.78	3.49%	0.02%	^{13}C	122.2	25.05%	2.53%
	Ratio	σ			Ratio	σ	
Si/(Si+Al+P)	0.194	0.00079		Si/(Si+Al+P)	0.337	0.073	
Al/(Si+Al+P)	0.457			Al/(Si+Al+P)	0.286		
P/(Si+Al+P)	0.349			P/(Si+Al+P)	0.376		

17. Influence of Detector Efficiency

The LEAP 4000X HR local electrode atom probe equipped with laser pulsing capabilities and an energy compensating reflectron lens has a detector efficiency of ~37%. The recently released LEAP 5000 XS has a detector efficiency of ~80%, and we were able to access this instrument at the CAMECA factory to test how the higher efficiency influences APT's ability to detect Si islands. Needles 10 and 11 are from the LEAP 5000 XS study, which was done on the template containing SAPO-34. Compared to the other template containing needles studied with the LEAP 4000X HR (needles 6-9), a similar composition is observed with the LEAP 5000 XS (Table S4). The Si NNDs for needles 10 and 11 were fit with a Gaussian function, and the peak maximum was at 0.53 nm for both needles, showing good agreement between two different experiments on that instrument. Needle 6 (run on a LEAP 4000X HR with a ~37% detector efficiency) showed a Gaussian Si NND centered at 0.63 nm, larger than the data collected with a LEAP 5000 XS. The larger value for the NND is expected due to the lower detector efficiency. A direct comparison of the Si NND from needle 6 from the LEAP 4000X HR and needle 11 from the LEAP 5000 XS is shown in Figure S20, highlighting the shift to lower Si-pair distances with increased efficiency, though there was no significant deviation from a random distribution in either case. The Si RDFs were also combined for needles 10-11, and are compared with the combined RDFs of needles 6-9 in Figure S12, but no significant difference can be found between these. The main manuscript discusses that this is likely due to the fact that spatial blurring dominates any contribution of increased detector efficiency in the range studied when clusters of small numbers of ions are considered in a matrix containing a significant solute concentration.

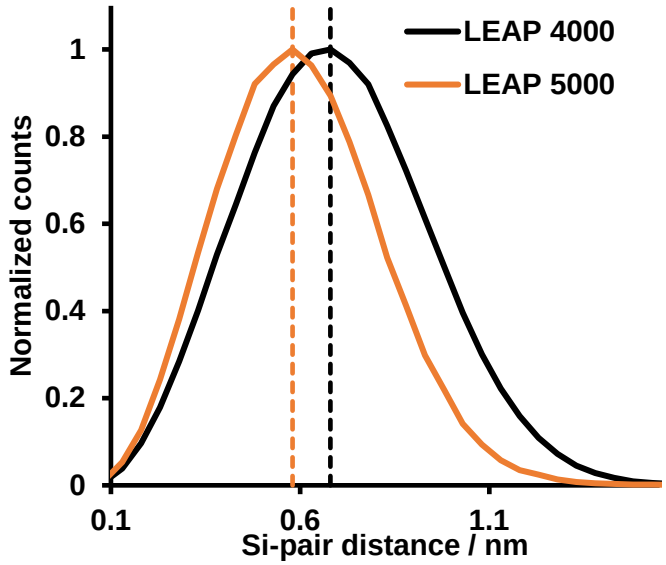

Figure S20. Comparison of Si nearest neighbor distributions (NNDs) for the LEAP 4000 (needle 6) and LEAP 5000 (needle 11). The maximum of the Gaussian distribution is indicated for both instruments to illustrate the shorter Si-pair distance with higher detection efficiency.

18. Atom Probe Tomography Simulations

In our recent review article, we presented simulations to show that we believe the spatial resolution of APT could be no better than 0.25 nm when applied to MMs, much lower than the often-quoted values of 0.04 nm in depth and 0.20 nm laterally, and this is likely due to molecular evaporations, non-conductivity and nano-porosity of the material.[63,81–85] We then extended the simulation method to incorporate different tetrahedral (T_d) atoms. The simulation workflow was as follows:

1. The composition used for the simulations was such that 20% of all T_d atoms were Si, with all other T atoms representing Al or P. Islands of 5, 8, 14, and 31 Si atoms were inserted into 3*1*1, 2*2*1, 2*2*2, 3*3*2 packings of the unit cell of CHA, respectively, Si islands were inserted such that 25% of the silicon was in islands and 75% was isolated, regardless of island size and consistent with the NMR results.
2. The island-containing cells of SAPO-34 were packed using the diffpy python package[86] to build a supercell that contains around one million atoms. In the supercell, randomly selected T_d atoms from regions not defined by Si islands were converted to isolated Si such that isolated Si made up around 15% of all the T_d atoms.
3. Each atom was randomly displaced in space based on a Gaussian probability density function centered at its original position to simulate the delocalization in 3-D space. The standard deviations of the Gaussian function used were 0, 0.05, 0.1, 0.25, 0.5, and 1 nm.
4. Atoms were then randomly selected and eliminated from the data to simulate APT detection efficiencies of 33%, 80%, and 100%. *Note that the efficiency was applied to the same displaced data set.* This is why the normalized RDFs are similar for the same island sizes and displacements (the absolute values differ by amounts consistent with the simulated efficiencies).
5. After the simulations, the data sets were processed using CAMECA's IVAS software in the same manner as experimentally collected atom probe data, but with the simplification that only 3 species were present in the MS: O, Si and T_d, where T_d is either Al or P as the tetrahedral elements besides Si. Due to this, the simulations do have an advantage over experimental data as there are no ambiguities in the MS identification and no background, which is a distinct challenge in analyzing the experimental data. Results are in Figure S21 and S22.

Previously, we demonstrated how quickly crystallographic information will be lost for zeolite catalysts due to spatial resolution limitations.[63] As Figure S21 shows, when σ=0 nm the complete crystallographic data is conserved (note the views of the Si atoms are slightly rotated so that all Si ions can be seen). The other σ shown in this figure is 1 nm, though the ability to visualize pores is lost well before this. The real importance of these simulations is the NNDs and RDFs for Si in order to determine at which values of N_{Si}, σ and ε that indications of Si islands disappear. When NNDs and RDFs are examined, it is apparent that ε has the least significant influence on the results. It serves to shift the NND maximum to slightly larger values, as would be expected due to fewer atoms per unit volume, as well as reducing the number of counts for the NND, besides this ε does not significantly affect the ability to detect Si islands. This observation is consistent with the experimental results of comparing the LEAP 4000X HR and LEAP 5000 XS instruments, where the higher collection efficiency of the LEAP 5000 XS leads to a shorter Si-pair distance (Figure S20), though does not lead to much of an increased ability to detect Si islands, at least for the efficiencies simulated. When comparing the RDFs of each instrument for σ=0 nm and all island sizes there is no difference in the bulk normalized concentration as a function of distance from Si as the data sets have a large number of ions. The σ and N_{Si} values are the most influential parameters for determining Si-Si affinity detection, outweighing the influence of ε. For all σ=0 nm data sets both the RDFs and NNDs show crystallographic ordering, which would be expected as this is a perfect crystal lattice. When examining Figure S21a and b, it is clear that the crystallographic information is retained, especially in the RDFs, as the nearest neighbor is always O, followed by Si or T_d, and then a slightly higher Si-Si affinity at longer distances for the 31 atom islands, though not for distances much longer than 1 nm as any affinity will be quickly averaged over a large volume in 3-D space. It is important to note that the randomized NNDs will also show crystallographic order as the randomization is done by species and not by position. At σ=0.05 and 0.1 nm the RDFs still show crystallographic ordering as O is seen as the nearest neighbor, but at greater values of σ information regarding the crystallographic nearest neighbor is lost, and the normalized O concentration becomes its bulk value throughout, regardless of island size or ε. At these values of σ=0.05 and 0.1 nm the NNDs also reflect the heterogeneous Si distribution. At σ=0.25 nm, a clear Si-Si affinity is still observed in the RDFs at all island sizes, but it is more pronounced for larger islands. However, the NNDs no longer show a clear separation between the collected and randomized data, illustrating that even at σ=0.25 nm one of the key markers of heterogeneity no longer indicates Si-Si affinity. At σ=0.5 nm, a Si-Si affinity is still present in the RDFs, though is much lower in magnitude than at lower values of σ, and is more pronounced with larger islands, as expected, and the NNDs do not show any deviation from random. The highest value of σ simulated, 1 nm, leads to the loss of any Si-Si affinity in the RDFs except for the largest simulated island size, 31 atoms, yet even this is nearly insignificant in magnitude.

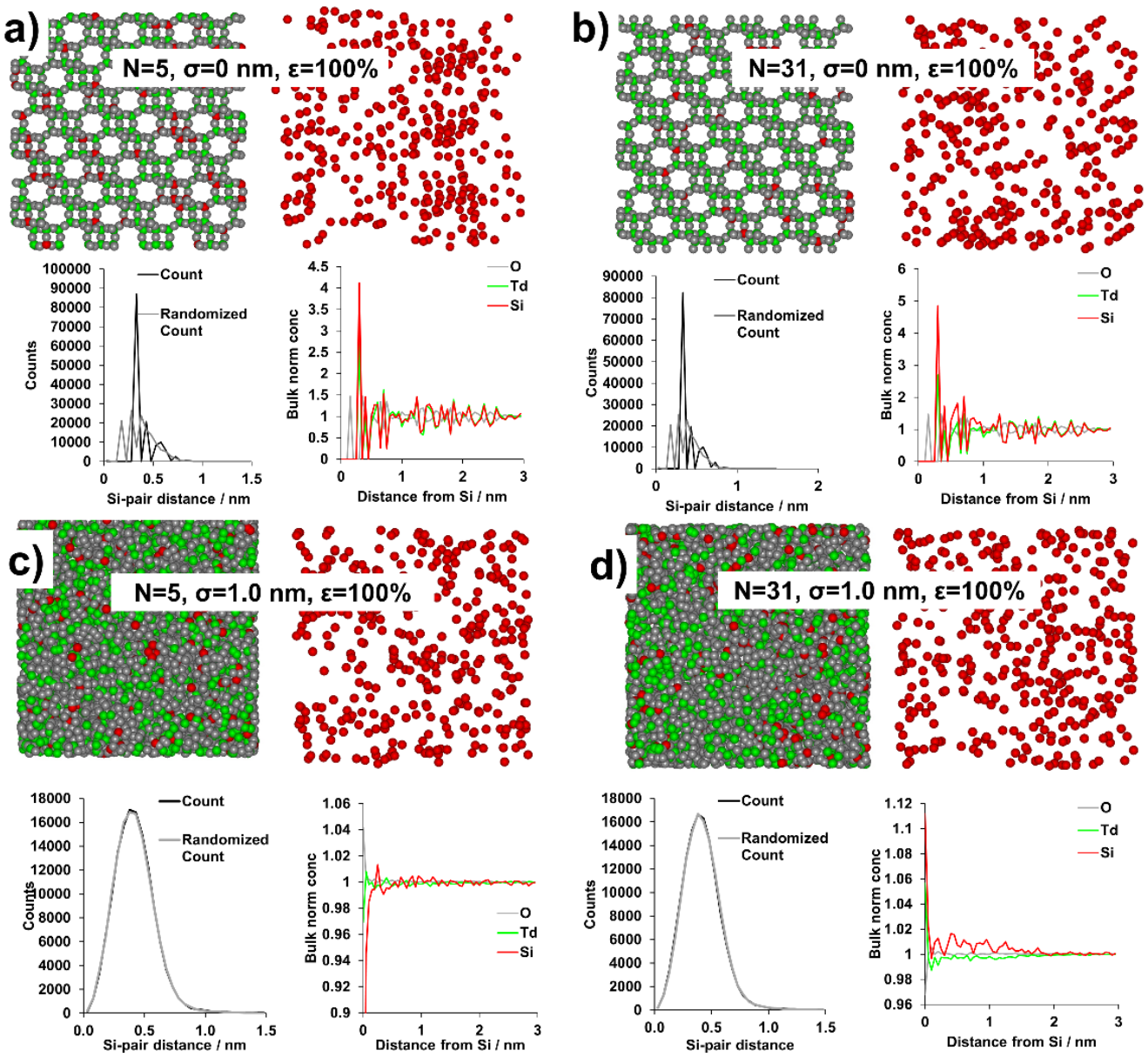

Figure S21. Selected results of atom probe simulations as a function of Si island size (N_{Si}) and delocalization (σ). Each panel contains a 5 × 5 × 5 nm^3 view of all atoms that was removed from the center of the larger simulated data set, as well as a view of only the Si atoms, with colors as shown in the radial distribution function (RDF) graph. Also shown are the nearest neighbor distributions (NNDs) for Si and the RDF for Si. Only 100% detection efficiency (ε) is shown as this parameter did not have a considerable influence on the results. Full results for all values of N_{Si}, σ and ε can be found in Figure S22. a) N_{Si}=5, σ=0 nm and ε=100%. b) N_{Si}=31, σ=0 nm and ε=100%. c) N_{Si}=5, σ=1.0 nm and ε=100%. d) N_{Si}=31, σ=1.0 nm and ε=100%. Note in a and b the views with only Si atoms have been slightly rotated compared to the view with all atoms so all Si atoms within the region of interest can be seen. Movies of the ion distributions for the 4 simulations are included as Movie S3.

N_{Si}=5, σ=0 nm, ε=100%

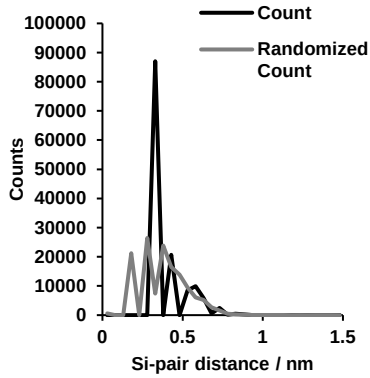

N_{Si}=5, σ=0 nm, ε=100%

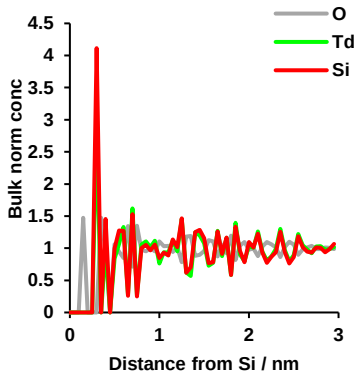

N_{Si}=5, σ=0 nm, ε=80%

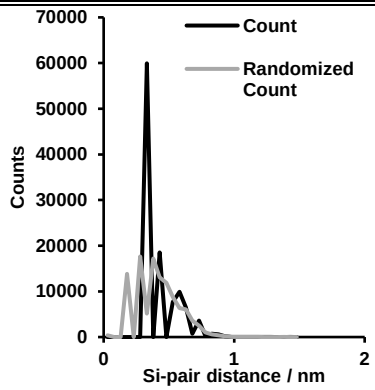

N_{Si}=5, σ=0 nm, ε=80%

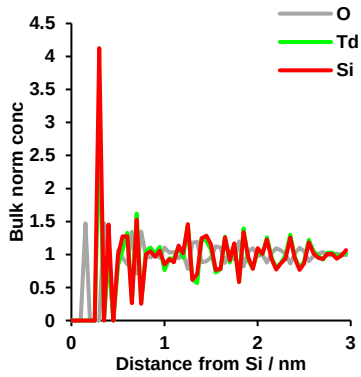

N_{Si}=5, σ=0 nm, ε=33%

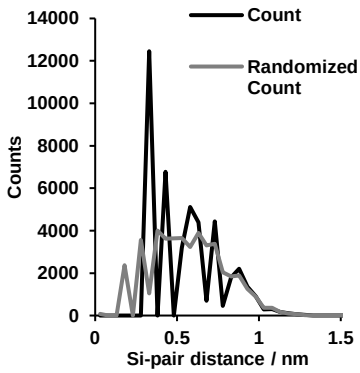

N_{Si}=5, σ=0 nm, ε=33%

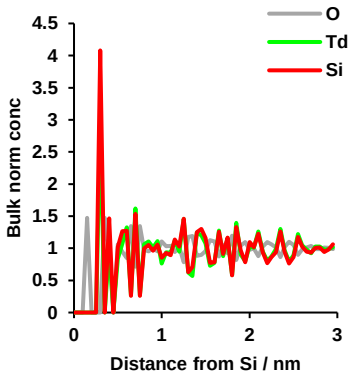

N_{Si}=5, σ=0.05 nm, ε=100%

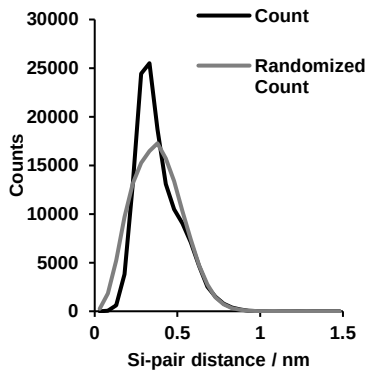

N_{Si}=5, σ=0.05 nm, ε=100%

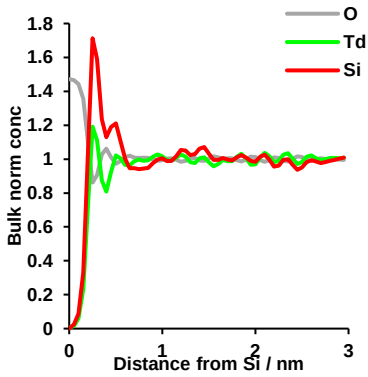

N_{Si}=5, σ=0.05 nm, ε=80%

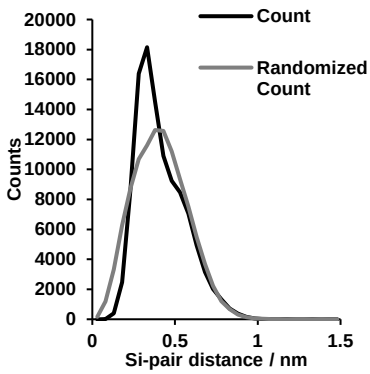

N_{Si}=5, σ=0.05 nm, ε=80%

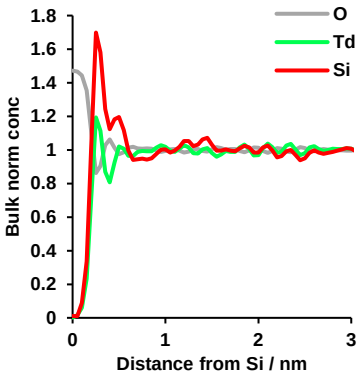

N_{Si}=5, σ=0.05 nm, ε=33%

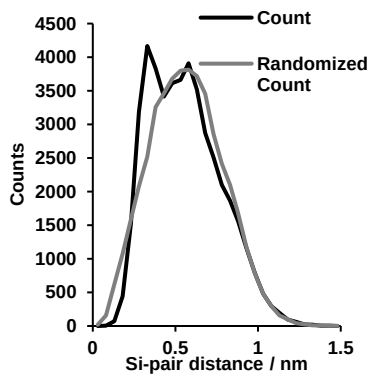

N_{Si}=5, σ=0.05 nm, ε=33%

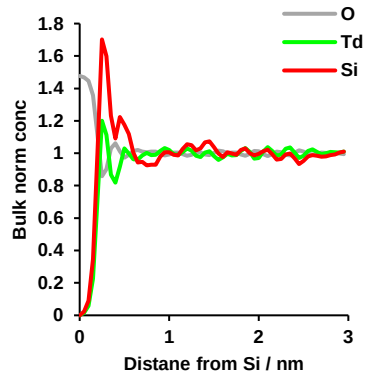

N_{Si}=5, σ=0.1 nm, ε=100%

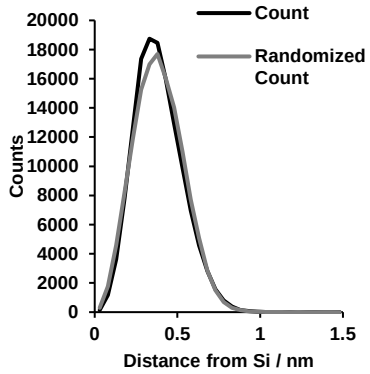

N_{Si}=5, σ=0.1 nm, ε=100%

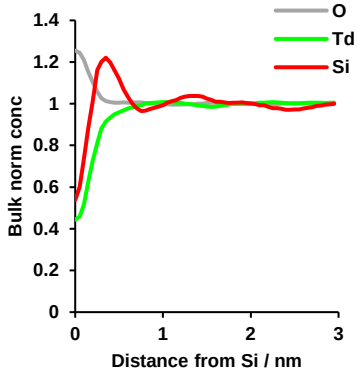

N_{Si}=5, σ=0.1 nm, ε=80%

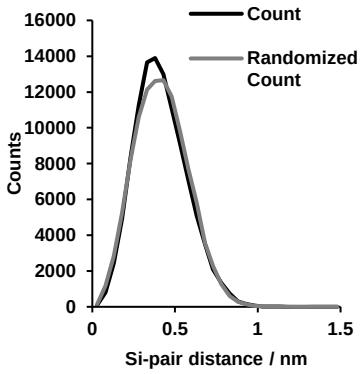

N_{Si}=5, σ=0.1 nm, ε=80%

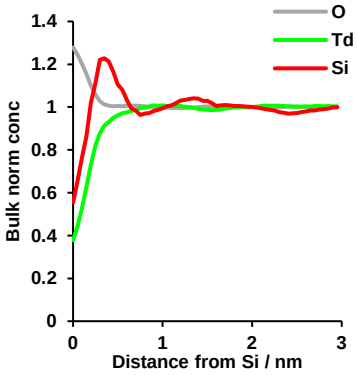

N_{Si}=5, σ=0.1 nm, ε=33%

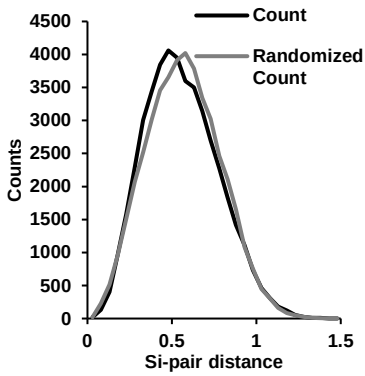

N_{Si}=5, σ=0.1 nm, ε=33%

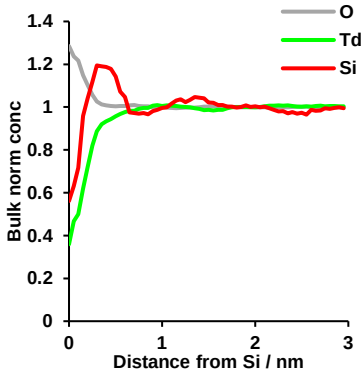

N_{Si}=5, σ=0.25 nm, ε=100%

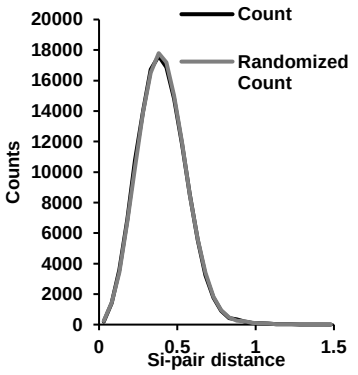

N_{Si}=5, σ=0.25 nm, ε=100%

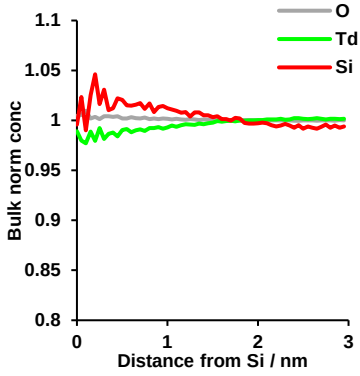

N_{Si}=5, σ=0.25 nm, ε=80%

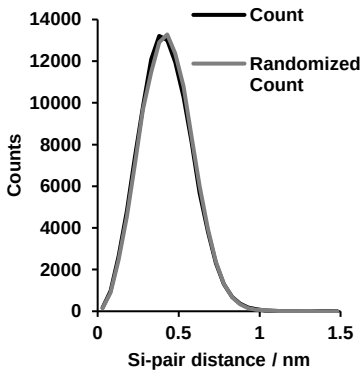

N_{Si}=5, σ=0.25 nm, ε=80%

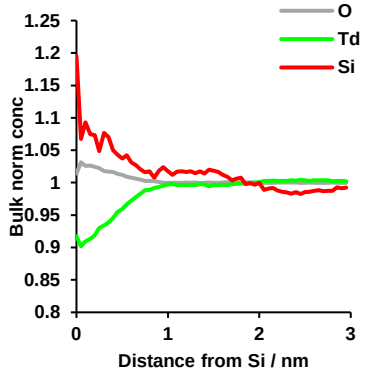

N_{Si}=5, σ=0.25 nm, ε=33%

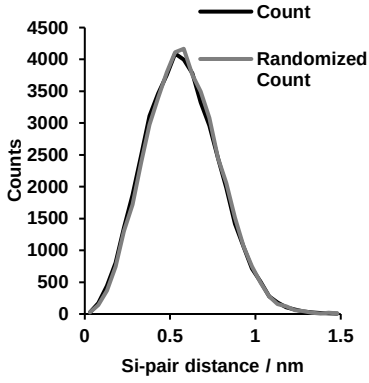

N_{Si}=5, σ=0.25 nm, ε=33%

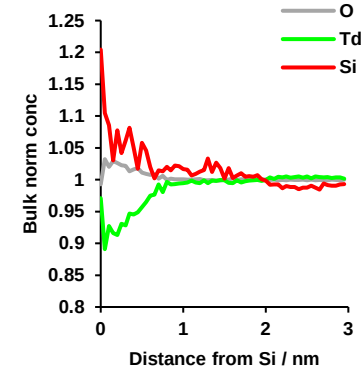

N_{Si}=5, σ=0.5 nm, ε=100%

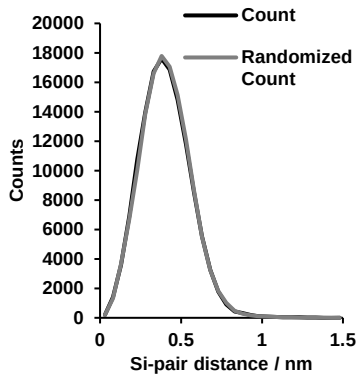

N_{Si}=5, σ=0.5 nm, ε=100%

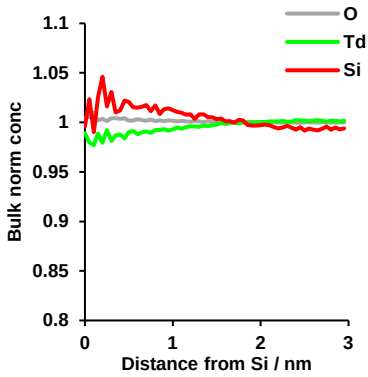

N_{Si}=5, σ=0.5 nm, ε=80%

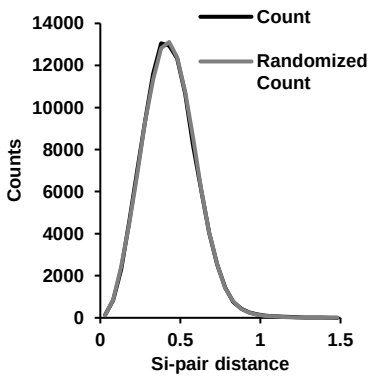

N_{Si}=5, σ=0.5 nm, ε=80%

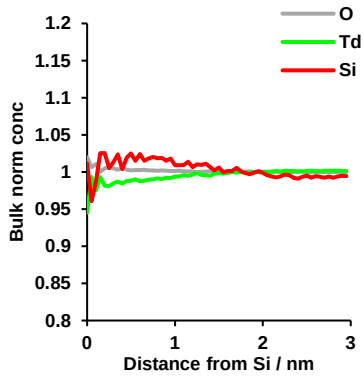

N_{Si}=5, σ=0.5 nm, ε=33%

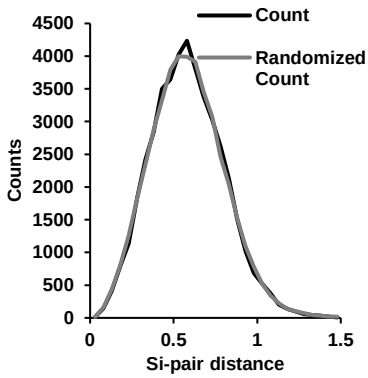

N_{Si}=5, σ=0.5 nm, ε=33%

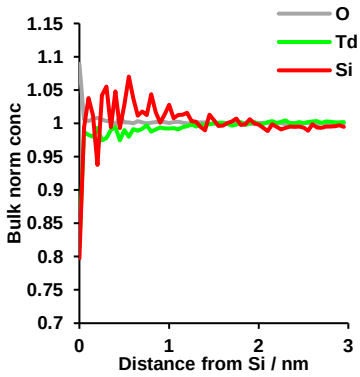

N_{Si}=5, σ=1 nm, ε=100%

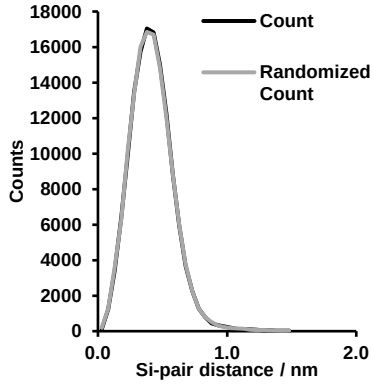

N_{Si}=5, σ=1 nm, ε=100%

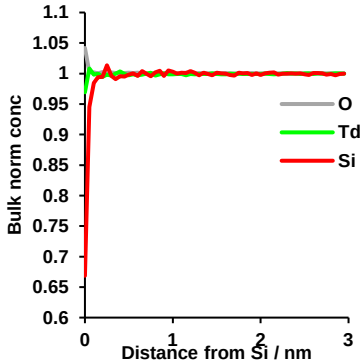

N_{Si}=5, σ=1 nm, ε=80%

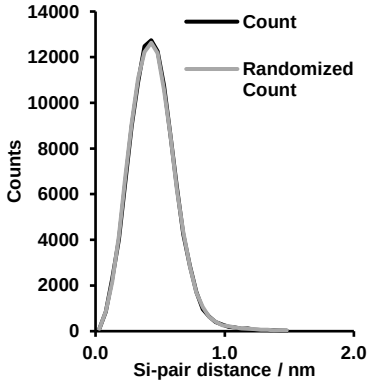

N_{Si}=5, σ=1 nm, ε=80%

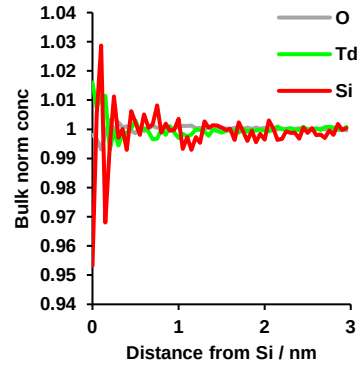

N_{Si}=5, σ=1 nm, ε=33%

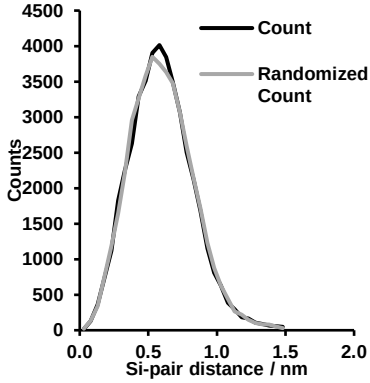

N_{Si}=5, σ=1 nm, ε=33%

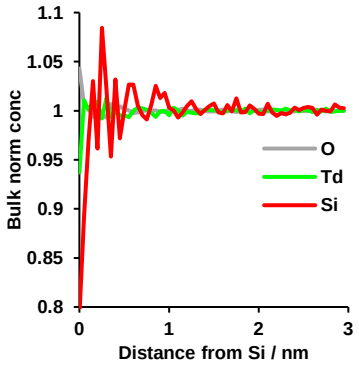

N_{Si}=8, σ=0 nm, ε=100%

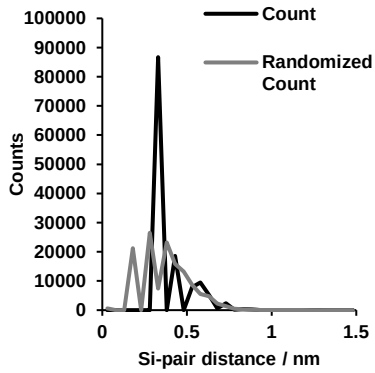

N_{Si}=8, σ=0 nm, ε=100%

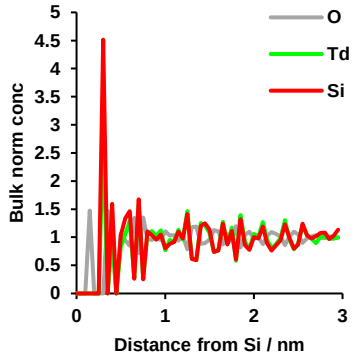

N_{Si}=8, σ=0 nm, ε=80%

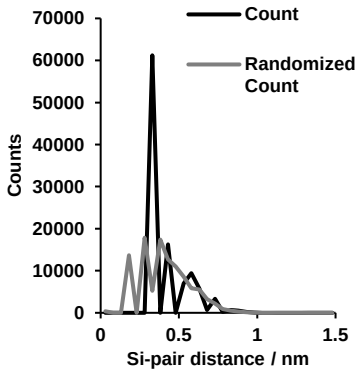

N_{Si}=8, σ=0 nm, ε=80%

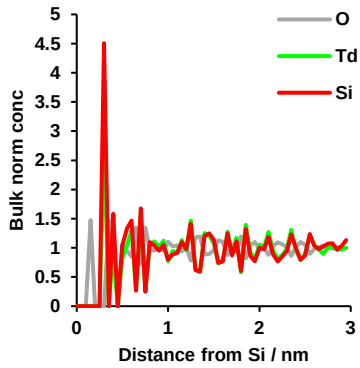

N_{Si}=8, σ=0 nm, ε=33%

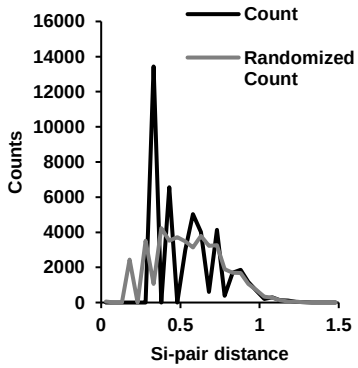

N_{Si}=8, σ=0 nm, ε=33%

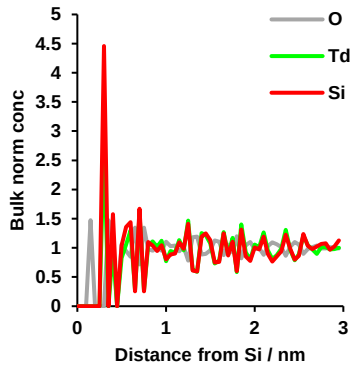

N_{Si}=8, σ=0.05 nm, ε=100%

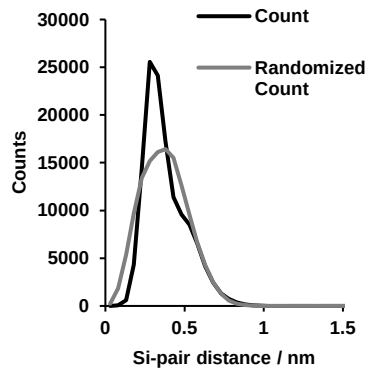

N_{Si}=8, σ=0.05 nm, ε=100%

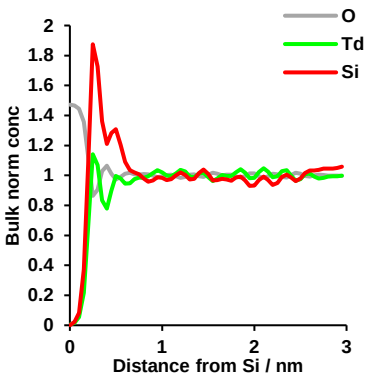

N_{Si}=8, σ=0.05 nm, ε=80%

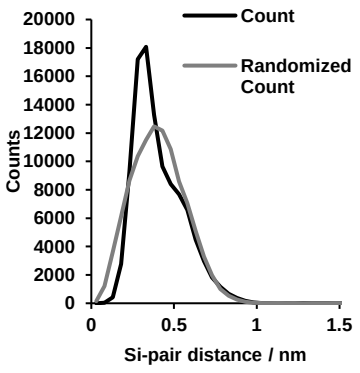

N_{Si}=8, σ=0.05 nm, ε=80%

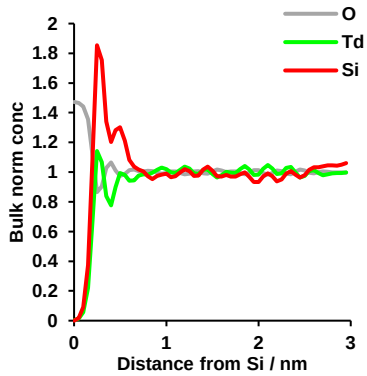

N_{Si}=8, σ=0.05 nm, ε=33%

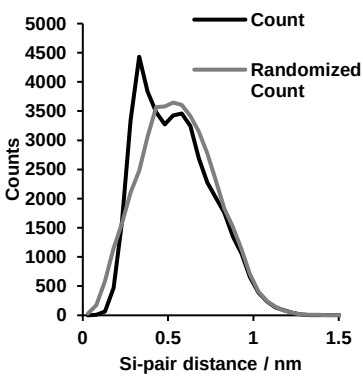

N_{Si}=8, σ=0.05 nm, ε=33%

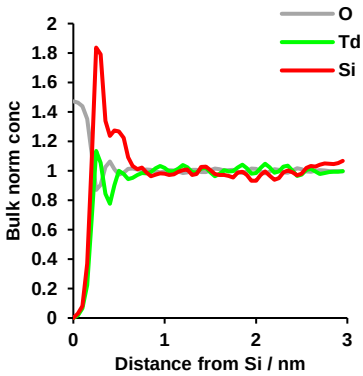

N_{Si}=8, σ=0.1 nm, ε=100%

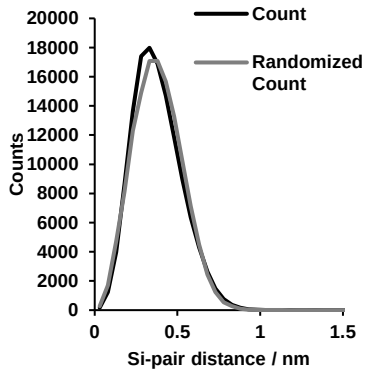

N_{Si}=8, σ=0.1 nm, ε=100%

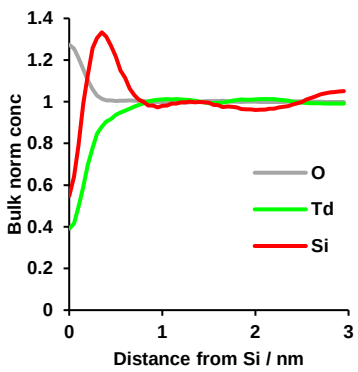

N_{Si}=8, σ=0.1 nm, ε=80%

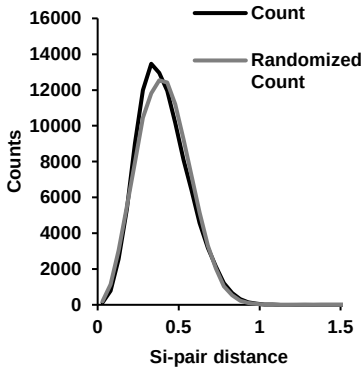

N_{Si}=8, σ=0.1 nm, ε=80%

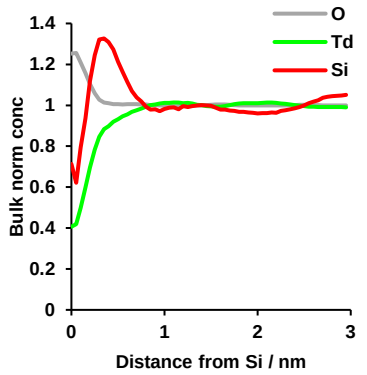

N_{Si}=8, σ=0.1 nm, ε=33%

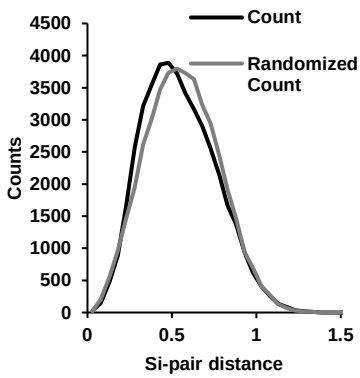

N_{Si}=8, σ=0.1 nm, ε=33%

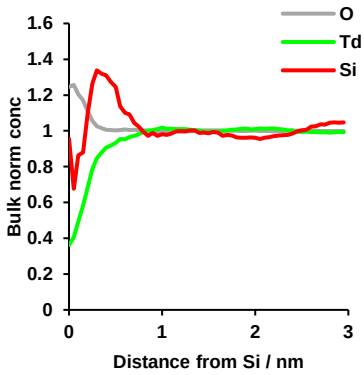

N_{Si}=8, σ=0.25 nm, ε=100%

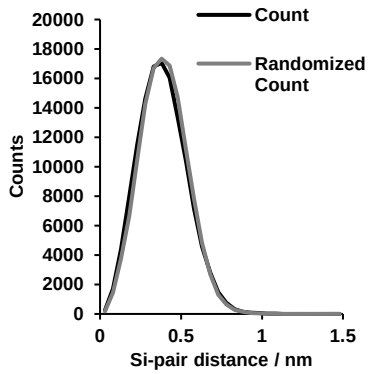

N_{Si}=8, σ=0.25 nm, ε=100%

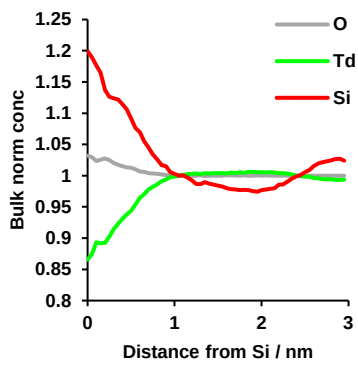

N_{Si}=8, σ=0.25 nm, ε=80%

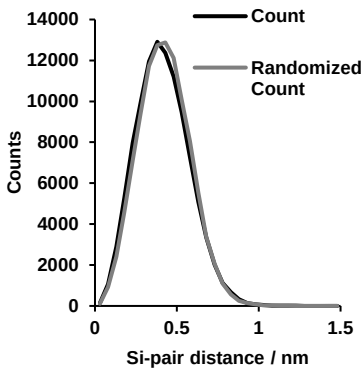

N_{Si}=8, σ=0.25 nm, ε=80%

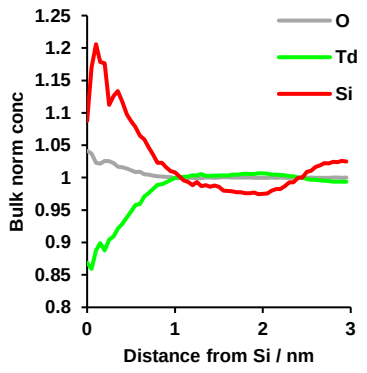

N_{Si}=8, σ=0.25 nm, ε=33%

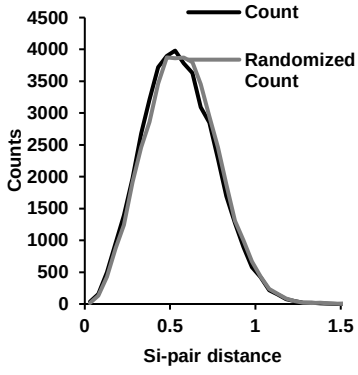

N_{Si}=8, σ=0.25 nm, ε=33%

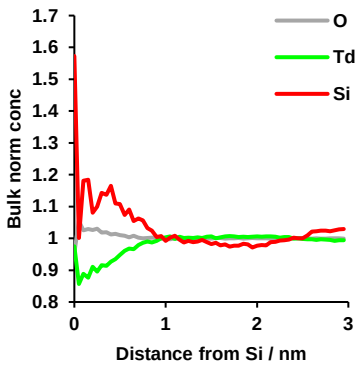

N_{Si}=8, σ=0.5 nm, ε=100%

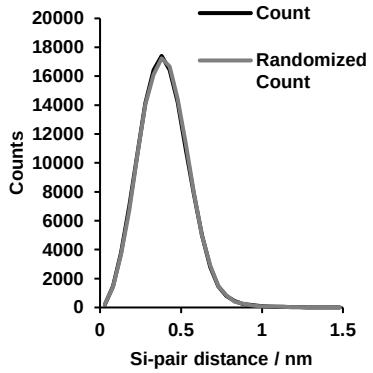

N_{Si}=8, σ=0.5 nm, ε=100%

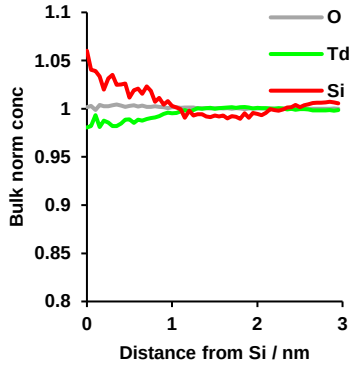

N_{Si}=8, σ=0.5 nm, ε=80%

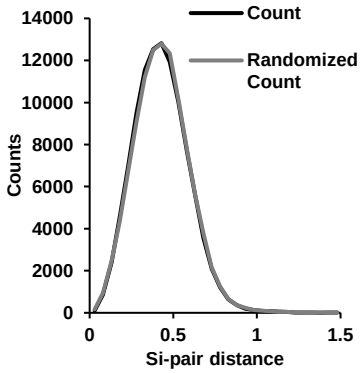

N_{Si}=8, σ=0.5 nm, ε=80%

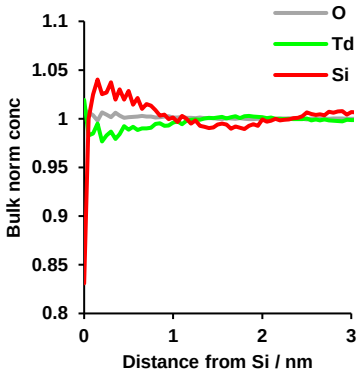

N_{Si}=8, σ=0.5 nm, ε=33%

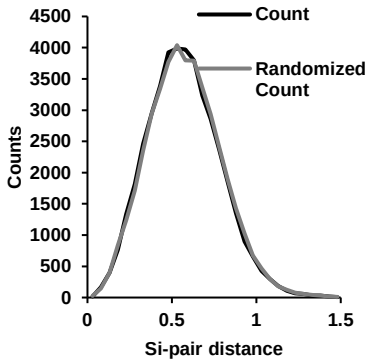

N_{Si}=8, σ=0.5 nm, ε=33%

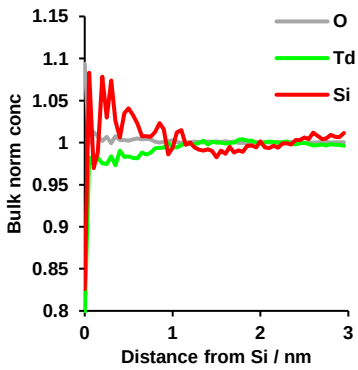

N_{Si}=8, σ=1 nm, ε=100%

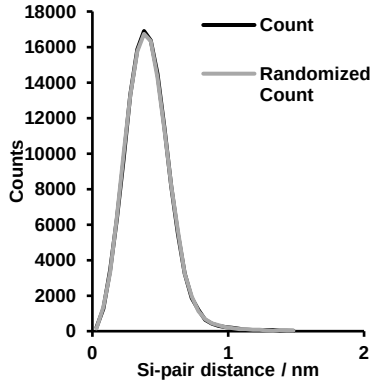

N_{Si}=8, σ=1 nm, ε=100%

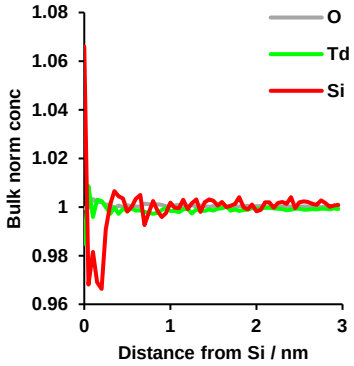

N_{Si}=8, σ=1 nm, ε=80%

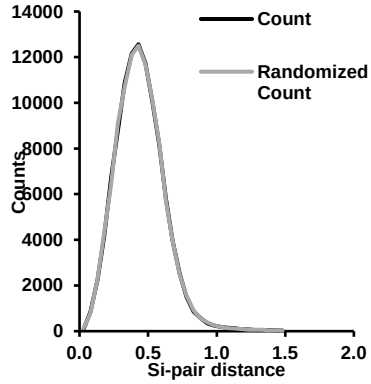

N_{Si}=8, σ=1 nm, ε=80%

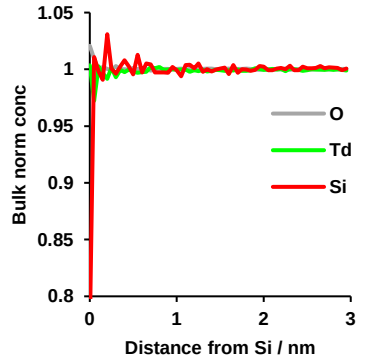

N_{Si}=8, σ=1 nm, ε=33%

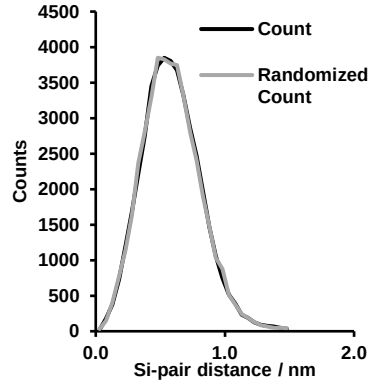

N_{Si}=8, σ=1 nm, ε=33%

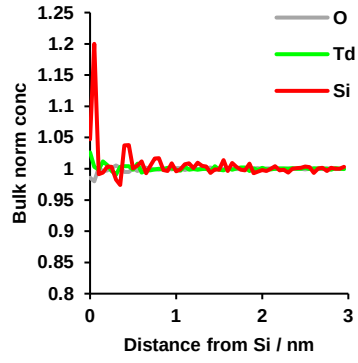

N_{Si}=14, σ=0 nm, ε=100%

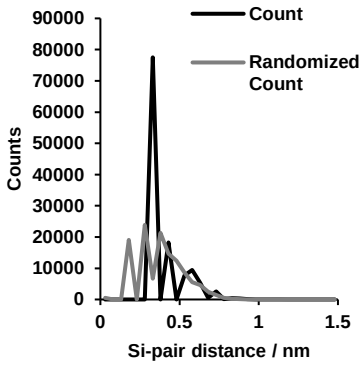

N_{Si}=14, σ=0 nm, ε=100%

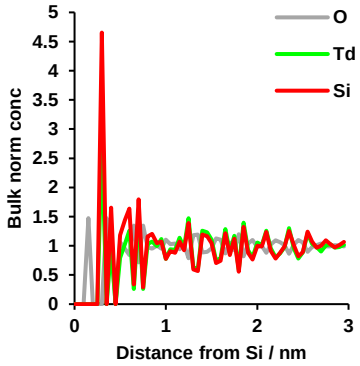

N_{Si}=14, σ=0 nm, ε=80%

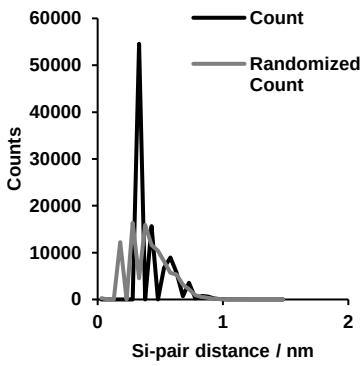

N_{Si}=14, σ=0 nm, ε=80%

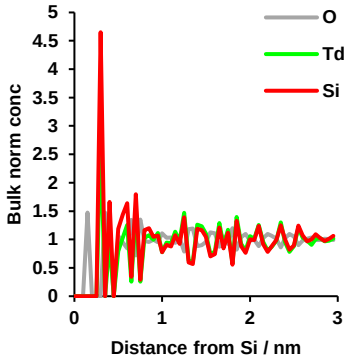

N_{Si}=14, σ=0 nm, ε=33%

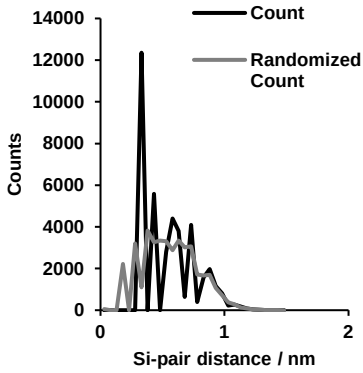

N_{Si}=14, σ=0 nm, ε=33%

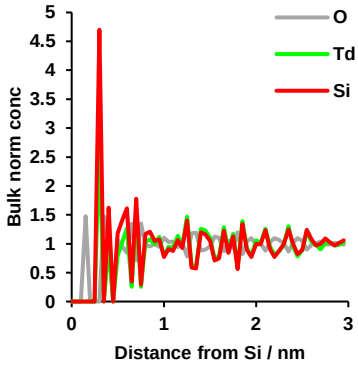

N_{Si}=14, σ=0.05 nm, ε=100%

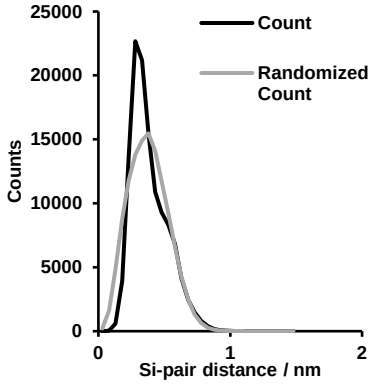

N_{Si}=14, σ=0.05 nm, ε=100%

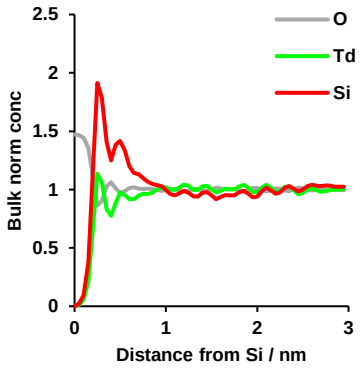

N_{Si}=14, σ=0.05 nm, ε=80%

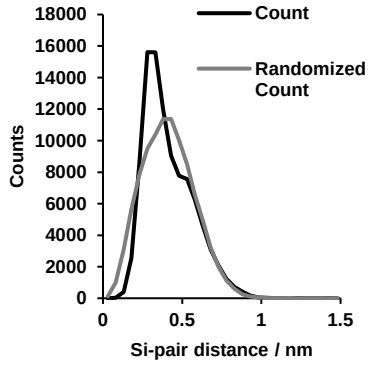

N_{Si}=14, σ=0.05 nm, ε=80%

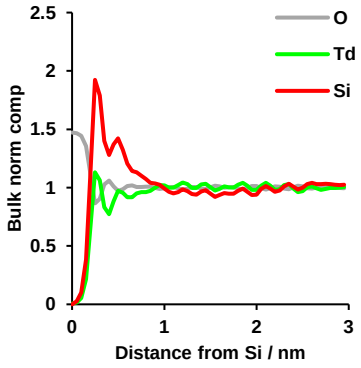

N_{Si}=14, σ=0.05 nm, ε=33%

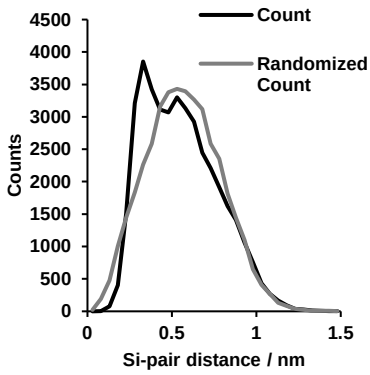

N_{Si}=14, σ=0.05 nm, ε=33%

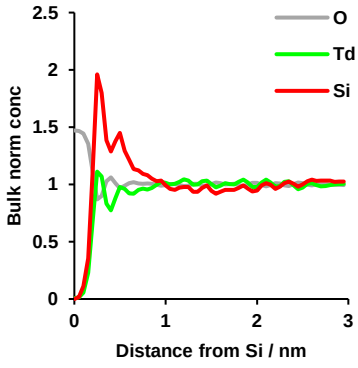

N_{Si}=14, σ=0.1 nm, ε=100%

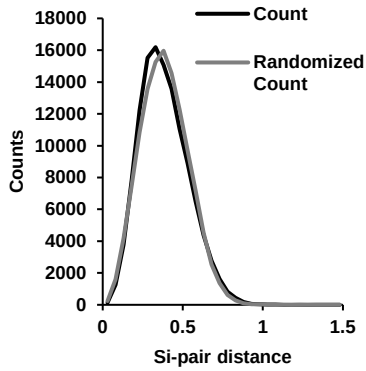

N_{Si}=14, σ=0.1 nm, ε=100%

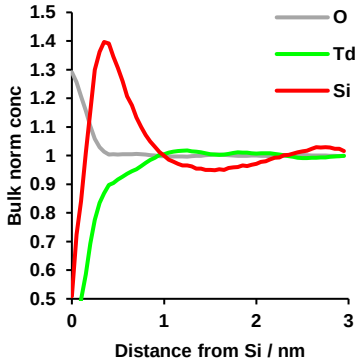

N_{Si}=14, σ=0.1 nm, ε=80%

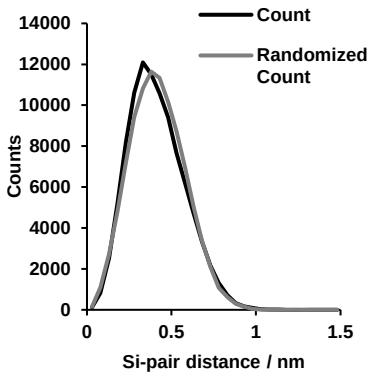

N_{Si}=14, σ=0.1 nm, ε=80%

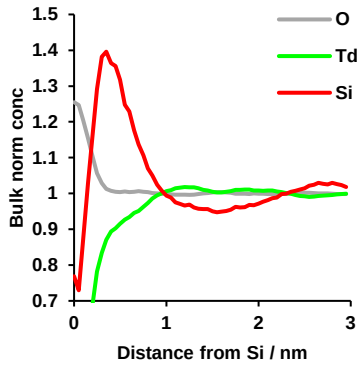

N_{Si}=14, σ=0.1 nm, ε=33%

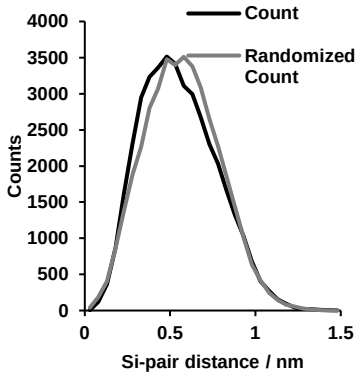

N_{Si}=14, σ=0.1 nm, ε=33%

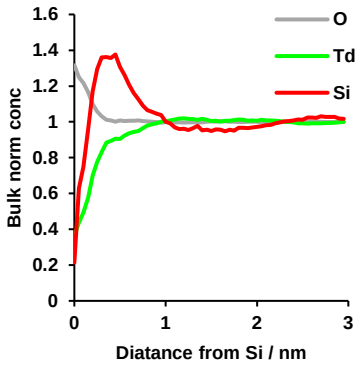

N_{Si}=14, σ=0.25 nm, ε=100%

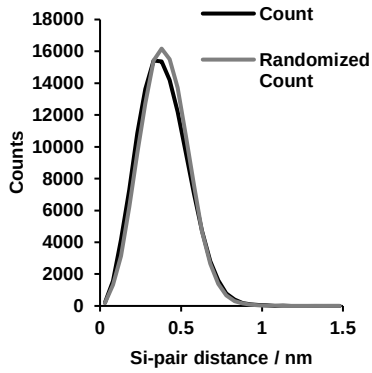

N_{Si}=14, σ=0.25 nm, ε=100%

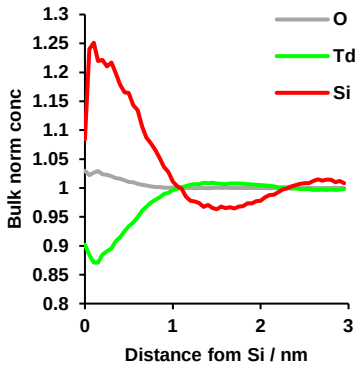

N_{Si}=14, σ=0.25 nm, ε=80%

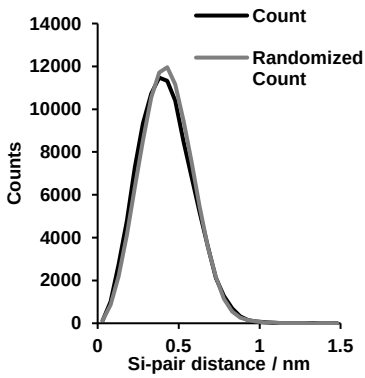

N_{Si}=14, σ=0.25 nm, ε=80%

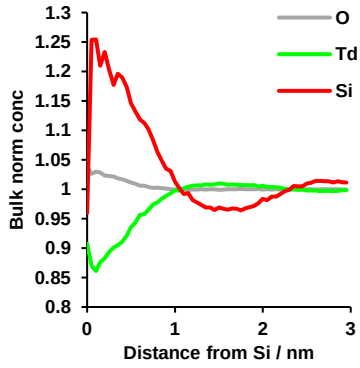

N_{Si}=14, σ=0.25 nm, ε=33%

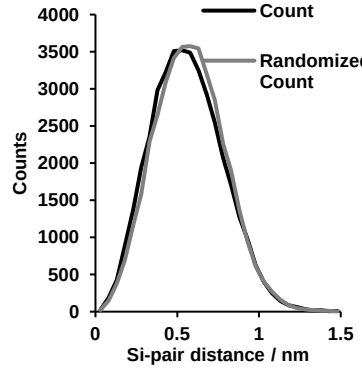

N_{Si}=14, σ=0.25 nm, ε=33%

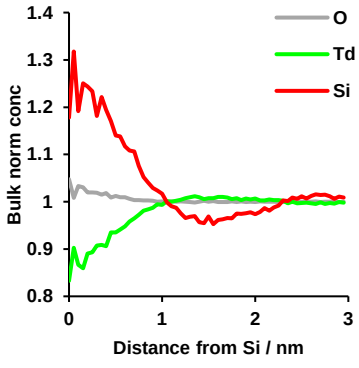

N_{Si}=14, σ=0.5 nm, ε=100%

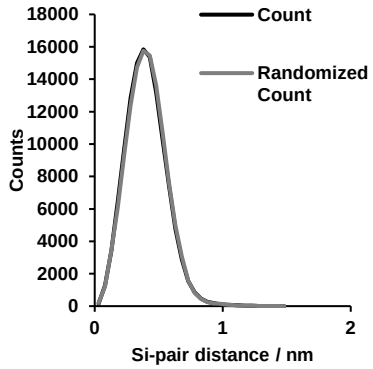

N_{Si}=14, σ=0.5 nm, ε=100%

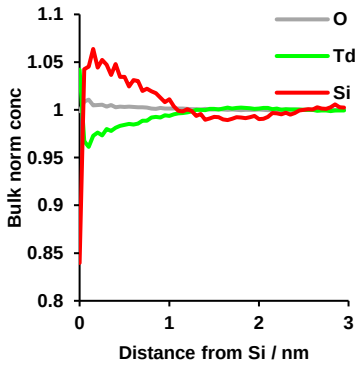

N_{Si}=14, σ=0.5 nm, ε=80%

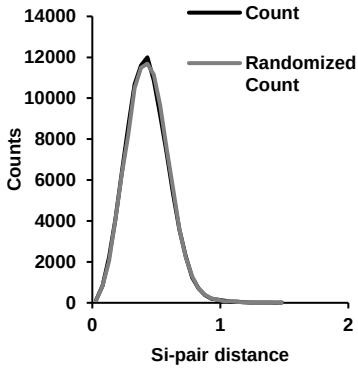

N_{Si}=14, σ=0.5 nm, ε=80%

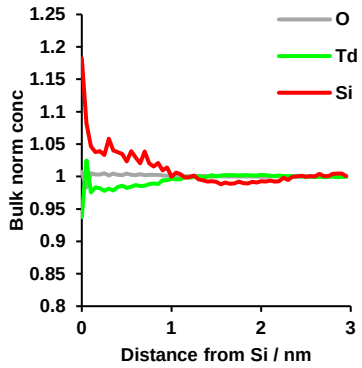

N_{Si}=14, σ=0.5 nm, ε=33%

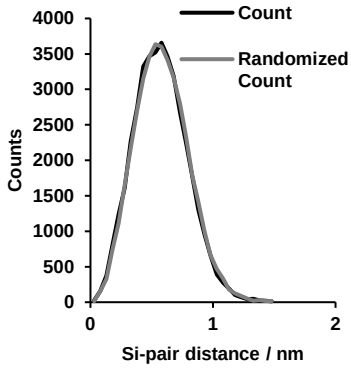

N_{Si}=14, σ=0.5 nm, ε=33%

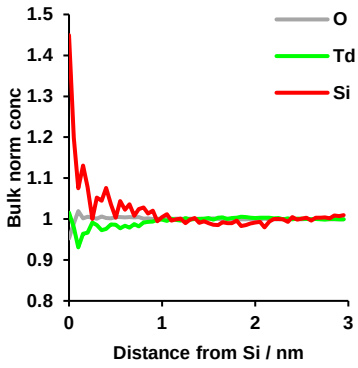

N_{Si}=14, σ=1 nm, ε=100%

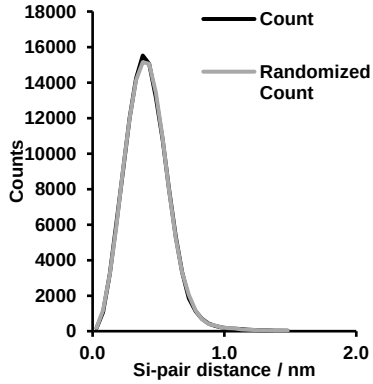

N_{Si}=14, σ=1 nm, ε=100%

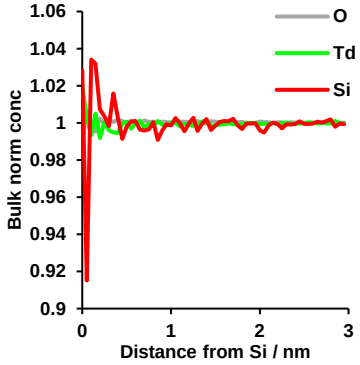

N_{Si}=14, σ=1 nm, ε=80%

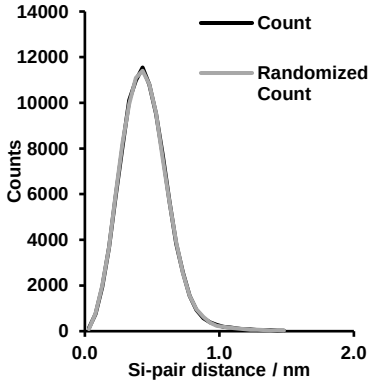

N_{Si}=14, σ=1 nm, ε=80%

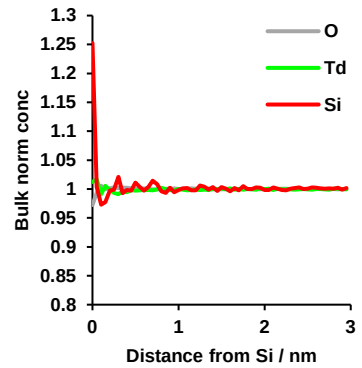

N_{Si}=14, σ=1 nm, ε=33%

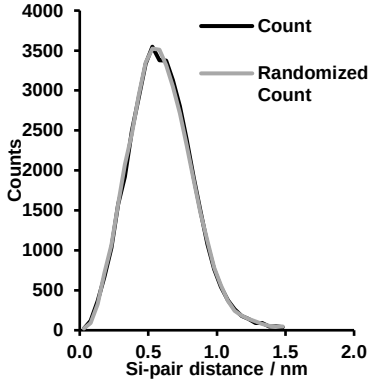

N_{Si}=14, σ=1 nm, ε=33%

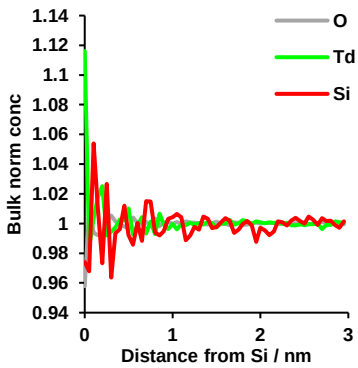

N_{Si}=31, σ=0 nm, ε=100%

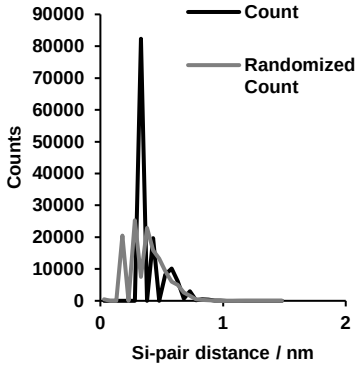

N_{Si}=31, σ=0 nm, ε=100%

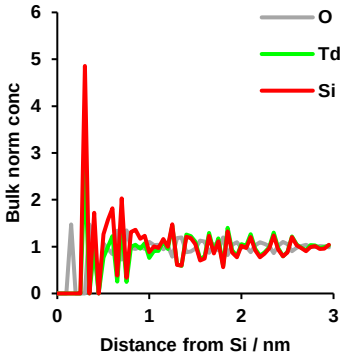

N_{Si}=31, σ=0 nm, ε=80%

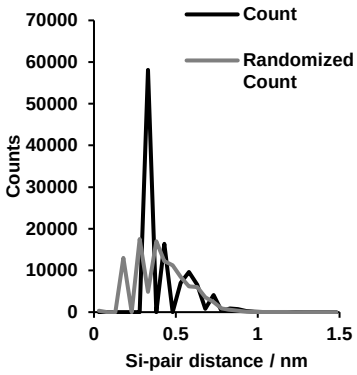

N_{Si}=31, σ=0 nm, ε=80%

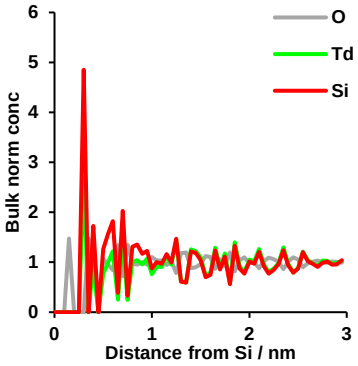

N_{Si}=31, σ=0 nm, ε=33%

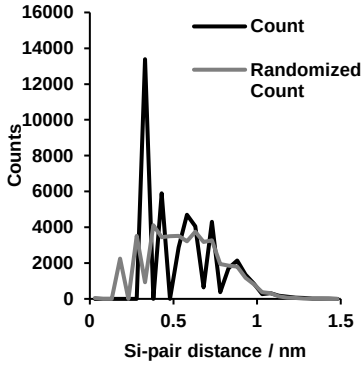

N_{Si}=31, σ=0 nm, ε=33%

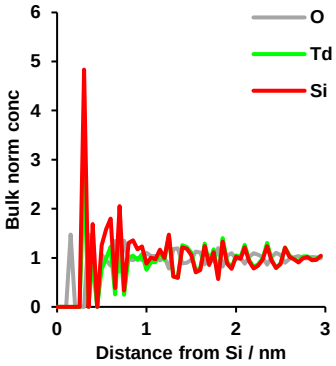

N_{Si}=31, σ=0.05 nm, ε=100%

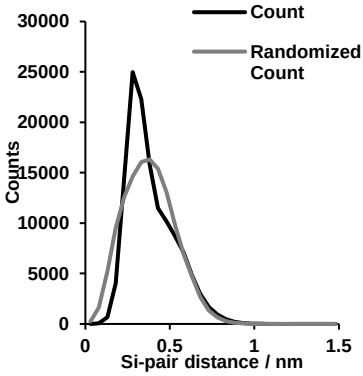

N_{Si}=31, σ=0.05 nm, ε=100%

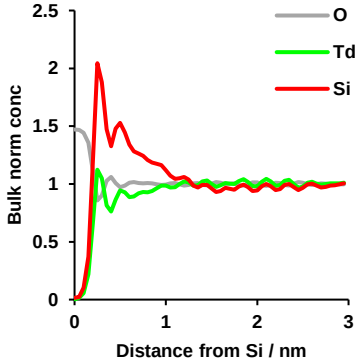

N_{Si}=31, σ=0.05 nm, ε=80%

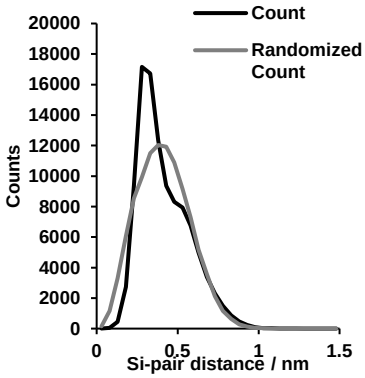

N_{Si}=31, σ=0.05 nm, ε=80%

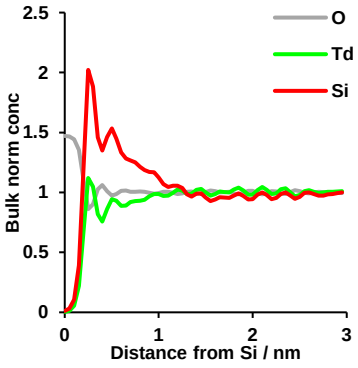

N_{Si}=31, σ=0.05 nm, ε=33%

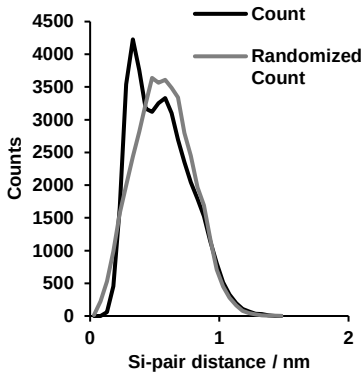

N_{Si}=31, σ=0.05 nm, ε=33%

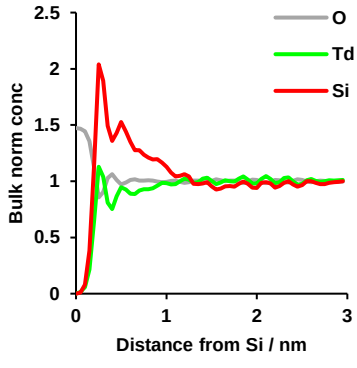

N_{Si}=31, σ=0.1 nm, ε=100%

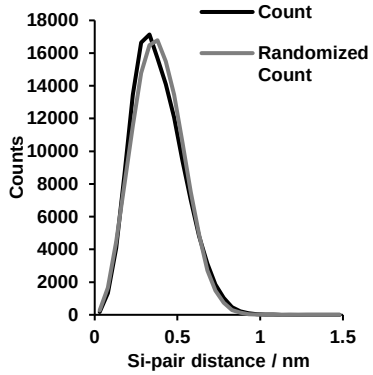

N_{Si}=31, σ=0.1 nm, ε=100%

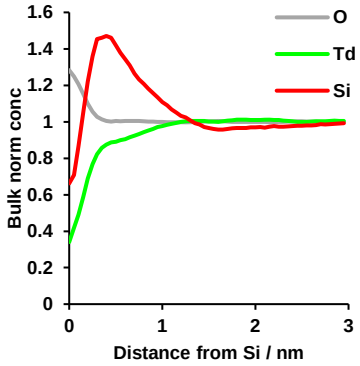

N_{Si}=31, σ=0.1 nm, ε=80%

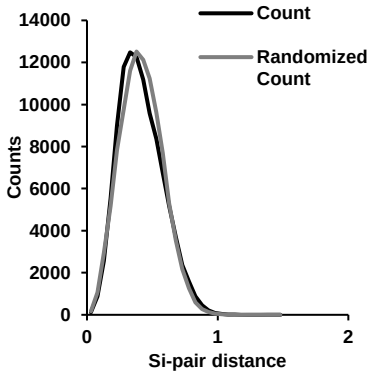

N_{Si}=31, σ=0.1 nm, ε=80%

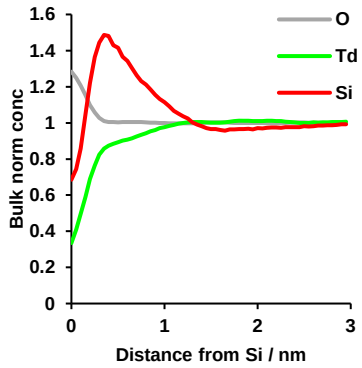

N_{Si}=31, σ=0.1 nm, ε=33%

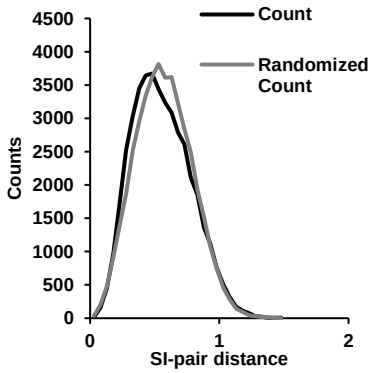

N_{Si}=31, σ=0.1 nm, ε=33%

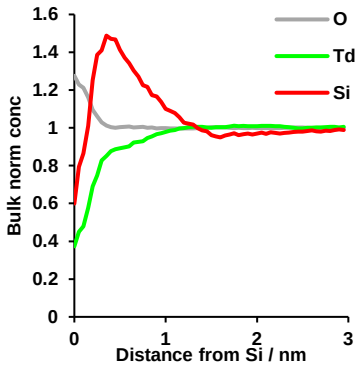

N_{Si}=31, σ=0.25 nm, ε=100%

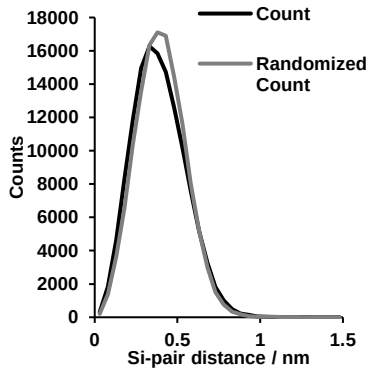

N_{Si}=31, σ=0.25 nm, ε=100%

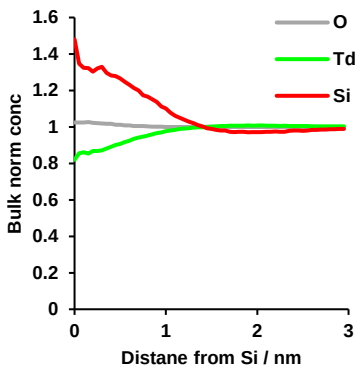

N_{Si}=31, σ=0.25 nm, ε=80%

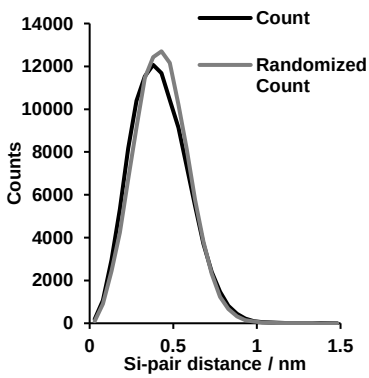

N_{Si}=31, σ=0.25 nm, ε=80%

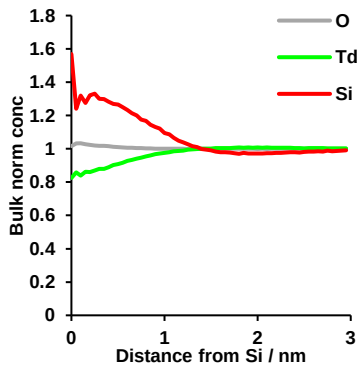

N_{Si}=31, σ=0.25 nm, ε=33%

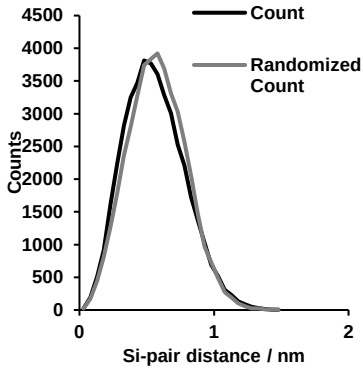

N_{Si}=31, σ=0.25 nm, ε=33%

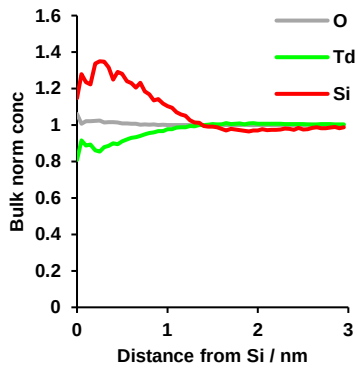

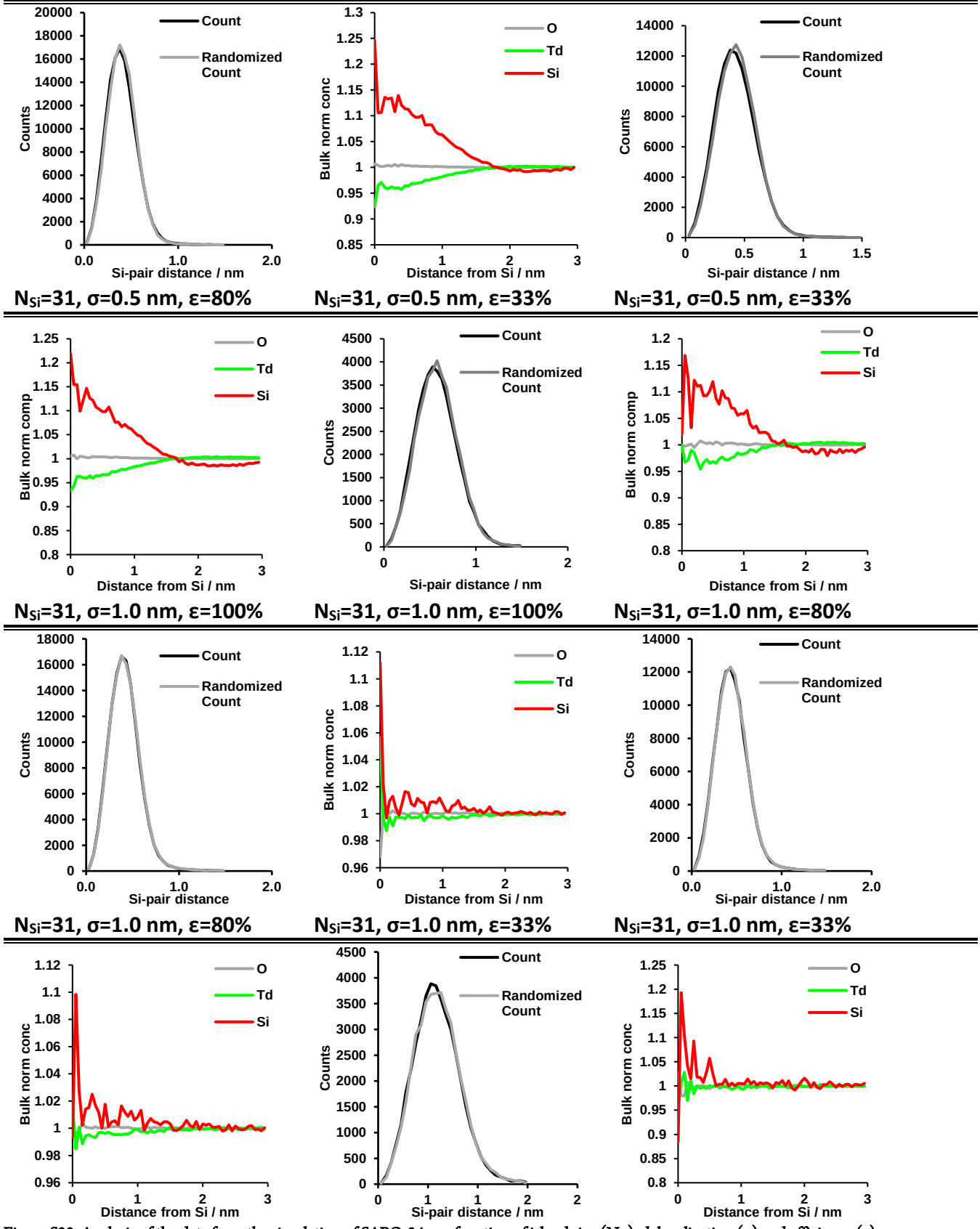

Figure S22. Analysis of the data from the simulation of SAPO-34 as a function of island size (N_{Si}), delocalization (σ) and efficiency (ε).

19. Supporting Information References

(1) Davis, M. E. Zeolites from a Materials Chemistry Perspective. *Chem. Mater.* **2014**, *26* (1), 239–245.
(2) Davis, M. E.; Lobo, R. F. Zeolite and Molecular Sieve Synthesis. *Chem. Mater.* **1992**, *4* (4), 756–768.
(3) Wilson, S. T.; Lok, B. M.; Messina, C. A.; Cannan, T. R.; Flanigen, E. M. Aluminophosphate Molecular Sieves: A New Class of Microporous Crystalline Inorganic Solids. *J. Am. Chem. Soc.* **1982**, *104* (4), 1146–1147.
(4) Lok, B. M.; Messina, C. A.; Patton, R. L.; Gajek, R. T.; Cannan, T. R.; Flanigen, E. M. Crystalline Silicoaluminophosphates. US Patent 4,440,871, 1984.
(5) Zheng, J.; Zhang, W.; Liu, Z.; Huo, Q.; Zhu, K.; Zhou, X.; Yuan, W. Unraveling the Non-Classic Crystallization of SAPO-34 in a Dry Gel System towards Controlling Meso-Structure with the Assistance of Growth Inhibitor: Growth Mechanism, Hierarchical Structure Control and Catalytic Properties. *Microporous Mesoporous Mater.* **2016**, *225*, 74–87.
(6) Sastre, G.; Lewis, D. W.; Catlow, C. R. A. Mechanisms of Silicon Incorporation in Aluminophosphate Molecular Sieves. *J. Mol. Catal. A Chem.* **1997**, *119* (1–3), 349–356.
(7) Ashtekar, S.; Chilukuri, S. V. V; Chakrabarty, D. K. Small-Pore Molecular Sieves SAPO-34 and SAPO-44 with Chabazite Structure: *J. Phys. Chem.* **1994**, *98*, 4878–4883.
(8) Flanigen, E. M.; Lok, B. M.; Patton, R. L.; Wilson, S. T. Aluminophosphate Molecular Sieves and the Periodic Table. *Stud. Surf. Sci. Catal.* **1986**, *28*, 103–112.
(9) Mertens, M.; Martens, J. A.; Grobet, P. J.; Jacobs, P. A. Effects of Substitution in SAPO-n Frameworks on Their Properties as Acid Catalysts. In *Guidelines for Mastering the Properties of Molecular Sieves*; Barthomeuf, D., Derouane, E. G., Hölderich, W., Eds.; Springer: Boston, 1990; pp 1–52.
(10) Barthomeuf, D. Topological Model for the Compared Acidity of SAPOs and SiAl Zeolites. *Zeolites* **1994**, *14* (6), 394–401.
(11) Appleyard, I. P.; Harris, R. K.; Fitch, F. R. Aluminum-27, Phosphorus-31, and Silicon-29 MAS NMR Studies of the Silicoaluminophosphate Molecular Sieve SAPO-5. *Chem. Lett.* **1985**, *14* (11), 1747–1750.
(12) Young, D.; Davis, M. Studies on SAPO-5: Synthesis with Higher Silicon Contents. *Zeolites* **1991**, *11* (3), 277–281.
(13) Man, P. P.; Briend, M.; Peltre, M. J.; Lamy, A.; Beaunier, P.; Barthomeuf, D. A Topological Model for the Silicon Incorporation in SAPO-37 Molecular Sieves: Correlations with Acidity and Catalysis. *Zeolites* **1991**, *11* (6), 563–572.
(14) Kühl, G. H.; Schmitt, K. D. A Reexamination of Phosphorus-Containing Zeolites ZK-21 and ZK-22 in Light of SAPO-42. *Zeolites* **1990**, *10* (1), 2–7.
(15) Vomscheid, R.; Peltre, M. J.; Barthomeup, D. The Role of the Template in Directing the Si Distribution in SAPO Zeolites. *J. Phys. Chem.* **1994**, *98* (38), 9614–9618.
(16) Arstad, B.; Lind, A.; Cavka, J. H.; Thorshaug, K.; Akporiaye, D.; Wragg, D.; Fjellvåg, H.; Grønvold, A.; Fuglerud, T. Structural Changes in SAPO-34 Due to Hydrothermal Treatment. A NMR, XRD, and DRIFTS Study. *Microporous Mesoporous Mater.* **2016**, *225*, 421–431.
(17) Jin, D.; Ye, G.; Zheng, J.; Yang, W.; Zhu, K.; Coppens, M.-O.; Zhou, X. Hierarchical Silicoaluminophosphate Catalysts with Enhanced Hydroisomerization Selectivity by Directing the Orientated Assembly of Premanufactured Building Blocks. *ACS Catal.* **2017**, *7* (9), 5887–5902.
(18) Sun, Q.; Xie, Z.; Yu, J. The State-of-the-Art Synthetic Strategies for SAPO-34 Zeolite Catalysts in Methanol-to-Olefin Conversion. *Natl. Sci. Rev.* **2017**, doi: 10.1093/nsr/nwx103.
(19) Vogt, C.; Weckhuysen, B. M.; Ruiz-Martínez, J. Effect of Feedstock and Catalyst Impurities on the Methanol-to-Olefin Reaction over H-SAPO-34. *ChemCatChem* **2017**, *9* (1), 183–194.
(20) Liu, G.; Tian, P.; Zhang, Y.; Li, J.; Xu, L.; Meng, S.; Liu, Z. Synthesis of SAPO-34 Templated by Diethylamine: Crystallization Process and Si Distribution in the Crystals. *Microporous Mesoporous Mater.* **2008**, *114* (1–3), 416–423.
(21) Iwase, Y.; Motokura, K.; Koyama, T.; Miyaji, A.; Baba, T. Influence of Si Distribution in Framework of SAPO-34 and Its Particle Size on Propylene Selectivity and Production Rate for Conversion of Ethylene to Propylene. *Phys. Chem. Chem. Phys.* **2009**, *11* (40), 9268–9277.
(22) Ye, L.; Cao, F.; Ying, W.; Fang, D.; Sun, Q. Effect of Different TEAOH/DEA Combinations on SAPO-34's Synthesis and Catalytic Performance. *J. Porous Mater.* **2011**, *18* (2), 225–232.
(23) Zhang, L.; Huang, Y. Crystallization and Catalytic Properties of Molecular Sieve SAPO-34 by a Vapor-Phase Transport Method. *J. Mater. Chem. A* **2015**, *3* (8), 4522–4529.
(24) Shen, W.; Li, X.; Wei, Y.; Tian, P.; Deng, F.; Han, X.; Bao, X. A Study of the Acidity of SAPO-34 by Solid-State NMR Spectroscopy. *Microporous Mesoporous Mater.* **2012**, *158*, 19–25.
(25) Li, Z.; Martínez-Triguero, J.; Concepción, P.; Yu, J.; Corma, A. Methanol to Olefins: Activity and Stability of Nanosized SAPO-34 Molecular Sieves and Control of Selectivity by Silicon Distribution. *Phys. Chem. Chem. Phys.* **2013**, *15* (35), 14670–14680.
(26) Zhang, L.; Huang, Y. New Insights into Formation of Molecular Sieve SAPO-34 for MTO Reactions. *J. Phys. Chem. C* **2016**, *120* (45), 25945–25957.
(27) Álvaro-Muñoz, T.; Márquez-Álvarez, C.; Sastre, E. Use of Different Templates on SAPO-34 Synthesis: Effect on the Acidity and Catalytic Activity in the MTO Reaction. *Catal. Today* **2012**, *179* (1), 27–34.
(28) Zhao, H.; Shi, S.; Wu, J.; Ding, Y.; Li, N. Charge Compensation Dominates the Distribution of Silica in SAPO-34. *Chinese J. Catal.* **2016**, *37* (2), 227–233.
(29) Suzuki, K.; Nishio, T.; Katada, N.; Sastre, G.; Niwa, M. Ammonia IRMS-TPD Measurements on Brønsted Acidity of Proton-Formed SAPO-34. *Phys. Chem. Chem. Phys.* **2011**, *13* (8), 3311–3318.
(30) Martínez-Franco, R.; Cantín, Á.; Vidal-Moya, A.; Moliner, M.; Corma, A. Self-Assembled Aromatic Molecules as Efficient Organic Structure Directing Agents to Synthesize the Silicoaluminophosphate SAPO-42 with Isolated Si Species. *Chem. Mater.* **2015**, *27* (8), 2981–2989.
(31) Martínez-Franco, R.; Li, Z.; Martínez-Triguero, J.; Moliner, M.; Corma, A. Improving the Catalytic Performance of SAPO-18 for the Methanol-to-Olefins (MTO) Reaction by Controlling the Si Distribution and Crystal Size. *Catal. Sci. Technol.* **2016**, *6* (8), 2796–2806.
(32) Pinilla-Herrero, I.; Márquez-Álvarez, C.; Sastre, E. Complex Relationship between SAPO Framework Topology, Content and Distribution of Si and Catalytic Behaviour in the MTO Reaction. *Catal. Sci. Technol.* **2017**, *7* (17), 3892–3901.
(33) Prakash, A. M.; Unnikrishnan, S. Synthesis of SAPO-34: High Silicon Incorporation in the Presence of Morpholine as Template. *J. Chem. Soc. Faraday Trans.* **1994**, *90* (15), 2291–2296.
(34) Tian, P.; Wei, Y.; Ye, M.; Liu, Z. Methanol to Olefins (MTO): From Fundamentals to Commercialization. *ACS Catal.* **2015**, *5* (3), 1922–1938.
(35) Briend, M.; Vomscheid, R.; Peltre, M. J.; Man, P. P.; Barthomeuf, D. Influence of the Choice of the Template on the Short- and Long-Term Stability of SAPO-34 Zeolite. *J. Phys. Chem.* **1995**, *99* (20), 8270–8276.
(36) Dai, W.; Wu, G.; Li, L.; Guan, N.; Hunger, M. Mechanisms of the Deactivation of SAPO-34 Materials with Different Crystal Sizes Applied as MTO Catalysts. *ACS Catal.* **2013**, *3* (4), 588–596.
(37) Bleken, F.; Bjørgen, M.; Palumbo, L.; Bordiga, S.; Svelle, S.; Lillerud, K.-P.; Olsbye, U. The Effect of Acid Strength on the Conversion of Methanol to Olefins Over Acidic Microporous Catalysts with the CHA Topology. *Top. Catal.* **2009**, *52* (3), 218–228.
(38) Hereijgers, B. P. C.; Bleken, F.; Nilsen, M. H.; Svelle, S.; Lillerud, K. P.; Bjørgen, M.; Weckhuysen, B. M.; Olsbye, U. Product Shape Selectivity Dominates the Methanol-to-Olefins (MTO) Reaction over H-SAPO-34 Catalysts. *J. Catal.* **2009**, *264* (1), 77–87.
(39) Lefevere, J.; Mullens, S.; Meynen, V.; Van Noyen, J. Structured Catalysts for Methanol-to-Olefins Conversion: A Review. *Chem. Pap.* **2014**, *68* (9), 1143–1153.

(40) Olsbye, U.; Svelle, S.; Bjørgen, M.; Beato, P.; Janssens, T. V. W.; Joensen, F.; Bordiga, S.; Lillerud, K. P. Conversion of Methanol to Hydrocarbons: How Zeolite Cavity and Pore Size Controls Product Selectivity. *Angew. Chem. Int. Ed.* **2012**, *51* (24), 5810–5831.
(41) Baerlocher, C.; McCusker, L. B. Database of Zeolite Structures, <http://www.iza-structure.org/databases/>. Accessed March 26, 2018.
(42) Dawson, D. M.; Griffin, J. M.; Seymour, V. R.; Wheatley, P. S.; Amri, M.; Kurkiewicz, T.; Guillou, N.; Wimperis, S.; Walton, R. I.; Ashbrook, S. E. A Multinuclear NMR Study of Six Forms of AlPO-34: Structure and Motional Broadening. *J. Phys. Chem. C* **2017**, *121* (3), 1781–1793.
(43) Wu, J.; Zhao, H.; Li, N.; Luo, Q.; He, C.; Guan, N.; Xiang, S. Fluorine-Free Crystallization of Triclinic AlPO4-34. *CrystEngComm* **2012**, *14* (24), 8671.
(44) Tuel, A.; Caldarelli, S.; Meden, A.; McCusker, L. B.; Baerlocher, C.; Ristic, A.; Rajic, N.; Mali, G.; Kaucic, V. NMR Characterization and Rietveld Refinement of the Structure of Rehydrated AlPO4-34. *J. Phys. Chem. B* **2000**, *104* (24), 5697–5705.
(45) Schunk, S. Element Distribution and Growth Mechanism of Large SAPO-5 Crystals. *Microporous Mater.* **1996**, *6* (5–6), 273–285.
(46) Chen, D.; Moljord, K.; Holmen, A. A Methanol to Olefins Review: Diffusion, Coke Formation and Deactivation on SAPO Type Catalysts. *Microporous Mesoporous Mater.* **2012**, *164*, 239–250.
(47) Aramburo, L. R.; Ruiz-Martínez, J.; Sommer, L.; Arstad, B.; Buitrago-Sierra, R.; Sepúlveda-Escribano, A.; Zandbergen, H. W.; Olsbye, U.; de Groot, F. M. F.; Weckhuysen, B. M. X-Ray Imaging of SAPO-34 Molecular Sieves at the Nanoscale: Influence of Steaming on the Methanol-to-Hydrocarbons Reaction. *ChemCatChem* **2013**, *5* (6), 1386–1394.
(48) Martens, J. A.; Mertens, M.; Grobet, P. J.; Jacobs, P. A. Synthesis and Characterisation of Silicon-Rich SAPO-5. In *Studies in Surface Science and Catalysis*; 1988; pp 97–105.
(49) Shwan, S.; Skoglundh, M.; Lundegaard, L. F.; Tiruvalam, R. R.; Janssens, T. V. W.; Carlsson, A.; Vennestrøm, P. N. R. Solid-State Ion-Exchange of Copper into Zeolites Facilitated by Ammonia at Low Temperature. *ACS Catal.* **2015**, *5* (1), 16–19.
(50) Morohoshi, K.; Miyazaki, T. Exhuast Gas Purification Catalyst. US Patent Application Number US2016/0263564 (A1). Filed Oct. 6, 2014.
(51) Nawaz, Z.; Tang, X.; Zhang, Q.; Wang, D.; Fei, W. SAPO-34 Supported Pt-Sn-Based Novel Catalyst for Propane Dehydrogenation to Propylene. *Catal. Commun.* **2009**, *10* (14), 1925–1930.
(52) Wang, D.; Jangjou, Y.; Liu, Y.; Sharma, M. K.; Luo, J.; Li, J.; Kamasamudram, K.; Epling, W. S. A Comparison of Hydrothermal Aging Effects on NH3-SCR of NOx over Cu-SSZ-13 and Cu-SAPO-34 Catalysts. *Appl. Catal. B Environ.* **2015**, *165*, 438–445.
(53) Ugurlu, O.; Haus, J.; Gunawan, A. A.; Thomas, M. G.; Maheshwari, S.; Tsapatsis, M.; Mkhoyan, K. A. Radiolysis to Knock-on Damage Transition in Zeolites under Electron Beam Irradiation. *Phys. Rev. B - Condens. Matter Mater. Phys.* **2011**, *83* (11), 113408.
(54) Bursill, L. A.; Thomas, J. M.; Rao, K. J. Stability of Zeolites under Electron Irradiation and Imaging of Heavy Cations in Silicates. *Nature* **1981**, *289*, 157–158.
(55) Mayoral, A.; Anderson, P. A.; Diaz, I. Zeolites Are No Longer a Challenge: Atomic Resolution Data by Aberration-Corrected STEM. *Micron* **2015**, *68*, 146–151.
(56) Karwacki, L.; Stavitski, E.; Kox, M. H. F.; Kornatowski, J.; Weckhuysen, B. M. Intergrowth Structure of Zeolite Crystals as Determined by Optical and Fluorescence Microscopy of the Template-Removal Process. *Angew. Chem. Int. Ed.* **2007**, *46* (38), 7228–7231.
(57) Marchese, L.; Frache, A.; Gianotti, E.; Martra, G.; Causà, M.; Coluccia, S. ALPO-34 and SAPO-34 Synthesized by Using Morpholine as Templating Agent. FTIR and FT-Raman Studies of the Host–guest and Guest–guest Interactions within the Zeolitic Framework. *Microporous Mesoporous Mater.* **1999**, *30* (1), 145–153.
(58) Fung, B. M.; Khitrin, A. K.; Ermolaev, K. An Improved Broadband Decoupling Sequence for Liquid Crystals and Solids. **2000**, *101*, 97–101.
(59) Tan, J.; Liu, Z.; Bao, X.; Liu, X.; Han, X.; He, C.; Zhai, R. Crystallization and Si Incorporation Mechanisms of SAPO-34. *Microporous Mesoporous Mater.* **2002**, *53* (1–3), 97–108.
(60) Xu, L.; Du, A.; Wei, Y.; Wang, Y.; Yu, Z.; He, Y.; Zhang, X.; Liu, Z. Synthesis of SAPO-34 with Only Si(4Al) Species: Effect of Si Contents on Si Incorporation Mechanism and Si Coordination Environment of SAPO-34. *Microporous Mesoporous Mater.* **2008**, *115* (3), 332–337.
(61) Schmidt, J. E.; Poplawsky, J. D.; Mazumder, B.; Attila, Ö.; Fu, D.; de Winter, D. A. M.; Meirer, F.; Bare, S. R.; Weckhuysen, B. M. Coke Formation in a Zeolite Crystal During the Methanol-to-Hydrocarbons Reaction as Studied with Atom Probe Tomography. *Angew. Chem. Int. Ed.* **2016**, *55* (37), 11173–11177.
(62) Poplawsky, J. D.; Schmidt, J. E.; Mazumder, B.; Guo, W.; Attila, Ö.; Fu, D.; de Winter, D. A. M.; Meirer, F.; Bare, S. R.; Weckhuysen, B. M. Nanoscale Chemical Imaging of Coking Mechanisms in a Zeolite ZSM-5 Crystal by Atom Probe Tomography. *Microsc. Microanal.* **2017**, *23* (S1), 674–675.
(63) Weckhuysen, B. M.; Schmidt, J.; Peng, L.; Poplawsky, J. Nanoscale Chemical Imaging of Zeolites Using Atom Probe Tomography. *Angew. Chem. Int. Ed.* **2018**, doi: 10.1002/anie.201712952.
(64) Thompson, K.; Lawrence, D.; Larson, D. J.; Olson, J. D.; Kelly, T. F.; Gorman, B. In Situ Site-Specific Specimen Preparation for Atom Probe Tomography. *Ultramicroscopy* **2007**, *107* (2–3), 131–139.
(65) Miller, M. K. *Atom Probe Tomography*; Springer US: Boston, MA, 2000.
(66) Larson, D. J.; Prosa, T. J.; Ulfig, R. M.; Geiser, B. P.; Kelly, T. F. *Local Electrode Atom Probe Tomography*; Springer: New York, 2013.
(67) La Fontaine, A.; Gault, B.; Breen, A.; Stephenson, L.; Ceguerra, A. V.; Yang, L.; Dinh Nguyen, T.; Zhang, J.; Young, D. J.; Cairney, J. M. Interpreting Atom Probe Data from Chromium Oxide Scales. *Ultramicroscopy* **2015**, *159*, 354–359.
(68) Sudbrack, C. K.; Noebe, R. D.; Seidman, D. N. Direct Observations of Nucleation in a Nondilute Multicomponent Alloy. *Phys. Rev. B* **2006**, *73* (21), 212101.
(69) Haley, D.; Petersen, T.; Barton, G.; Ringer, S. P. Influence of Field Evaporation on Radial Distribution Functions in Atom Probe Tomography. *Philos. Mag.* **2009**, *89* (11), 925–943.
(70) Philippe, T.; De Geuser, F.; Duguay, S.; Lefebvre, W.; Cojocaru-Mirédin, O.; Da Costa, G.; Blavette, D. Clustering and Nearest Neighbour Distances in Atom-Probe Tomography. *Ultramicroscopy* **2009**, *109* (10), 1304–1309.
(71) Miller, M. K.; Forbes, R. G. Atom Probe Tomography. *Mater. Charact.* **2009**, *60* (6), 461–469.
(72) Kelly, T. F.; Miller, M. K. Invited Review Article: Atom Probe Tomography. *Rev. Sci. Instrum.* **2007**, *78* (3), 031101.
(73) Miller, M. K.; Kelly, T. F.; Rajan, K.; Ringer, S. P. The Future of Atom Probe Tomography. *Mater. Today* **2012**, *15* (4), 158–165.
(74) Miller, M. K. *Atom Probe Tomography : Analysis at the Atomic Level*; Springer: New York, 2000.
(75) Rementeria, R.; Poplawsky, J. D.; Aranda, M. M.; Guo, W.; Jimenez, J. A.; Garcia-Mateo, C.; Caballero, F. G. Carbon Concentration Measurements by Atom Probe Tomography in the Ferritic Phase of High-Silicon Steels. *Acta Mater.* **2017**, *125*, 359–368.
(76) Ku, H. H. Notes on the Use of Propagation of Error Formulas. *J. Res. Natl. Bur. Stand. Sect. C Eng. Instrum.* **1966**, *70C* (4), 263-273.
(77) Mores, D.; Stavitski, E.; Kox, M. H. F.; Kornatowski, J.; Olsbye, U.; Weckhuysen, B. M. Space- And Time-Resolved in-Situ Spectroscopy on the Coke Formation in Molecular Sieves: Methanol-to-Olefin Conversion over H-ZSM-5 and H-SAPO-34. *Chem. - A Eur. J.* **2008**, *14* (36), 11320–11327.
(78) Qian, Q.; Ruiz-Martínez, J.; Mokhtar, M.; Asiri, A. M.; Al-Thabaiti, S. A.; Basahel, S. N.; van der Bij, H. E.; Kornatowski, J.; Weckhuysen, B. M. Single-Particle Spectroscopy on Large SAPO-34 Crystals at Work: Methanol-to-Olefin versus Ethanol-to-Olefin Processes. *Chem. - A Eur. J.* **2013**, *19* (34), 11204–11215.
(79) Qian, Q.; Ruiz-Martínez, J.; Mokhtar, M.; Asiri, A. M.; Al-Thabaiti, S. A.; Basahel, S. N.; Weckhuysen, B. M. Single-Catalyst Particle Spectroscopy of Alcohol-to-Olefins Conversions: Comparison between SAPO-34 and SSZ-13. *Catal. Today* **2014**, *226*, 14–24.
(80) Qian, Q.; Ruiz-Martínez, J.; Mokhtar, M.; Asiri, A. M.; Al-Thabaiti, S. A.; Basahel, S. N.; Weckhuysen, B. M. Single-Particle Spectroscopy of Alcohol-to-Olefins over SAPO-34 at Different Reaction Stages: Crystal Accessibility and Hydrocarbons Reactivity. *ChemCatChem* **2014**, *6* (3), 772–783.

(81) Gault, B.; Moody, M. P.; Cairney, J. M.; Ringer, S. P. *Atom Probe Microscopy*; Springer Series in Materials Science; Springer New York, 2012; Vol. 160.
(82) Vurpillot, F.; Da Costa, G.; Menand, A.; Blavette, D. Structural Analyses in Three-Dimensional Atom Probe: A Fourier Transform Approach. *J. Microsc.* **2001**, *203* (3), 295–302.
(83) Vurpillot, F.; De Geuser, F.; Da Costa, G.; Blavette, D. Application of Fourier Transform and Autocorrelation to Cluster Identification in the Three-Dimensional Atom Probe. *J. Microsc.* **2004**, *216* (3), 234–240.
(84) Gault, B.; Moody, M. P.; De Geuser, F.; La Fontaine, A.; Stephenson, L. T.; Haley, D.; Ringer, S. P. Spatial Resolution in Atom Probe Tomography. *Microsc. Microanal.* **2010**, *16* (01), 99–110.
(85) Devaraj, A.; Colby, R.; Hess, W. P.; Perea, D. E.; Thevuthasan, S. Role of Photoexcitation and Field Ionization in the Measurement of Accurate Oxide Stoichiometry by Laser-Assisted Atom Probe Tomography. *J. Phys. Chem. Lett.* **2013**, *4* (6), 993–998.
(86) Juhás, P.; Farrow, C. L.; Yang, X.; Knox, K. R.; Billinge, S. J. L. Complex Modeling: A Strategy and Software Program for Combining Multiple Information Sources to Solve Ill Posed Structure and Nanostructure Inverse Problems. *Acta Crystallogr. Sect. A Found. Adv.* **2015**, *71*, 562–568.